Experimental and Numerical Investigation of Micro/Mini Channel Flow-Boiling Heat Transfer with Non-Uniform Circumferential Heat Fluxes at Different Rotational Orientations

M Vermaak[1], J Potgieter[1], J Dirker[1], M A Moghimi[1], P Valluri[2], K Sefiane[2,3], J P Meyer[1]

[1] University of Pretoria, Pretoria, South Africa

[2] University of Edinburgh, Edinburgh, United Kingdom

[3]Tianjin Key Lab of Refrigeration Technology, Tianjin University of Commerce, Tianjin City 300134, PR China

Highlights

•Heat transfer coefficients in microchannels affected by rotational orientation
•Secondary buoyancy driven flow was observed experimentally and numerically
•Computational fluid dynamics was used to simulate bubble growth

Abstract Flow-boiling of Perfluorohexane (FC-72) in horizontal micro/mini channels was investigated experimentally and numerically at different rotational orientations in terms of gravity. One-sided uniform channel heating was considered experimentally for rotational angles ranging from 0° (heating from below) to 180° (heating from above) in increments of 30°. The micro/mini channel had a high aspect ratio of 10 (5 mm x 0.5 mm) and a hydraulic diameter of 909 μm. In-channel flow visualisations were recorded and heat transfer coefficients were determined for mass fluxes of 10, 20 and 40 kg/m^{2}s at a saturation temperature of 56 °C. Suitable heat fluxes were applied to span the onset of nucleate boiling to near dry-out conditions within the channel. It was found that the rotational angle had a significant influence on the heat transfer performance due to its influence on bubble detachment. Bottom-heated cases (0° orientation) resulted in local heat transfer coefficients that were up to 201% higher than for any other rotational orientation. Channel orientations of 60° (slanted heating surface) and 90° (heating from the side) generally produced the lowest local heat transfer coefficients. Insight into the influence of the gravitational orientation on single-bubble growth within the nucleation and detachment region was obtained via two- and three-dimensional numerical simulations. Bubble behaviour after detachment and its effect on heat transfer were also investigated transiently until detachment. The numerical simulations mirrored the experimental trends and it was found that the presence of growing bubbles interrupted the velocity streamlines and the thermal boundary layer downstream of the nucleation site.

Keywords: *flow-boiling, microchannel, rotational orientation, heat transfer coefficient*

Manuscript received February 2013, revised March 2013

Nomenclature

a	Heat loss coefficient
b	Heat loss exponent
BH	Bottom-heated rotation (θ = 0°)
c	Volume fraction
c_p	Specific heat (J/kg)
D	Diameter (m)
g	Gravity (m/s^2)
G	Mass flux (kg/m^{2}s)
h	Energy source term (W/m^3)
h_{fg}	Latent heat of vaporisation (J/kg)
I	Electric current (A)
k	Thermal conductivity (W/mK))
L	Length (m)
$\dot{m}$	Mass flow rate (kg/m^{2}s)
M	Molecular mass (kg/mol)
n	Unit normal
N_t	Normalisation factor
P	Pressure (Pa)
q	Effective heat flux (W/m^2)
$\dot{Q}$	Absorbed heat (W)
R	Gas constant (J/molK)
S	Source term (kg/m^{3}s)
t	Time (s)
t_{max}	Maximum time step size (s)
T	Temperature (°C)
TH	Top-heated rotation (θ = 180°)
u	Velocity (m/s)
U	Voltage (V)
$\dot{V}$	Volumetric flow rate (m^3/s)
W	Width (m)

Greek symbols

α	Heat transfer coefficient (W/m^{2}K)
δ	Kronecker delta function
Γ	Diffusion parameter
δ_L	Refinement level
δ_M	Refinement area
θ	Rotational angle (°)
θ_c	Contact angle (°)
κ	Curvature (m^{-1})
ρ	Density (kg/m^3)
$\dot{\rho}_{tr}$	Schrage mass transfer (kg/m^{3}s)
σ	Surface tension (N/m)
Φ	Scalar
χ	Vapour quality
ω	Accommodation coefficient

Subscripts

b	Bulk fluid condition
c	Cell condition
eff	Effective condition
l	Local condition in cross-section
$liquid$	Liquid phase
in	Internal passage condition
$inlet$	Inlet condition
h	Heated surface condition
0	Outer condition
$outlet$	Outlet condition
sat	Saturation condition
$vapour$	Vapour phase
w	Wall condition
z	Axial position

1. INTRODUCTION

Flow-boiling is a process by which heat is transferred from a surface within a flow passage while the fluid is undergoing a phase change and experiences bulk fluid motion. It has been investigated extensively due to its use in an extended set of applications ranging from large-scale to miniature systems. In large-scale systems, for instance, steam production is required in Rankine-type power cycles to drive steam turbines for electricity generation, while in nuclear

power applications, flow-boiling is used (among others) as a cooling mechanism. Whereas the latter applications utilise relatively large diameter flow passages, flow-boiling in small-scale passages is of particular interest to electronic cooling with high heat flux requirements.

Different flow-boiling applications may require different flow passage orientations in terms of gravity, or if not restricted, favourable orientations can be adopted to enhance the heat transfer performance by utilising the effects of buoyancy-driven flow. As such, it has been shown that heat transfer ability is dependent on the flow channel orientation, specifically in regions where the fluid is a two-phase mixture of liquid and vapour [1].

The two aspects that influence the overall orientation of a channel can be described in terms of the channel's relative inclination and the channel's relative rotational (azimuth) position. Inclination is commonly used to indicate the flow direction in relation to gravity and refers to situations such as upward flow, downward flow and horizontal flow. When a flow passage is significantly non-circular, and/or when it experiences circumferential non-uniform heating, and/or when buoyancy-driven flow effects are significant, the relative rotational orientation is used to refer to heating predominantly occurring from below, above or the side.

As mentioned, flow-boiling can occur in large flow passages as well as in small flow passages. Based on the fluid properties and the channel dimensions, indicators such as the confinement number [2], Bond number [3] and capillary length [4] can be used to broadly classify channels into three types: macrochannels, minichannels and microchannels. However, as a first-order approximation, channels with hydraulic diameters in the order of magnitude of less than 1 mm are sometimes referred to as microchannels. Each channel classification exhibits different dominant flow influences, which indirectly affect the heat transfer. At relatively low mass fluxes, and depending on the two-phase flow regime, macrochannels are affected almost entirely by gravity, while surface tension has a negligible effect. Minichannels are affected by both gravity and surface tension, while microchannels are predominantly affected by surface tension.

Due to the increased demand for electronic cooling, a significant proportion of flow-boiling research has been conducted on microchannels. For this application type, the channels are arranged as either a single channel or an array of parallel channels integrated into a heat sink. Generally, the application dictates that heating occurs on one side of the microchannel or heat sink. Specific refrigerants are often used and are selected based on their thermodynamic properties and fluid properties. Perfluorohexane (FC-72), for instance, is thermally and chemically stable, compatible with sensitive materials, non-flammable, non-toxic and leaves no residue upon evaporation [5]. Depending on the manufacturing method, cross-sectional channel profiles range from circular to approximately rectangular. Rectangular channels often have width-to-height ratios of between 0.33 and 20. Uniform surface heating conditions are often considered on the heated side. However, due to thermal conduction in the microchannel substrate, this inevitably results in some degree of circumferential non-uniform heat flux on the internal wetted surface. Studies have been conducted on the influence of parameters such as the number of channels [6, 7], the cross-sectional profile [8-10], hydraulic diameters [11-15], systems with uniform heating [16-22], the orientation of the channel [1, 23, 24], hydrodynamic effects like confinement [25-27] and the effect of varying working fluids [28, 29].

Inclination effects have been investigated extensively in macrochannels due to, for instance, its importance to the nuclear and other industries where horizontal and vertical flow passages are commonly found [22]. For macrochannels, rotational effects have also been investigated because of their importance in horizontal flow-boiling in, for instance, direct steam generation processes in the solar power industry where parabolic trough or Fresnel solar receivers [30] are utilised.

Some work has also been done on small-scale channels, focusing on the influence of the flow passage orientation on the heat transfer coefficients, pressure drop behaviour and flow instability. More advanced studies have aimed to create a correlation for the heat transfer coefficient with the data collected [31-34]. The parameters most often varied include the channel orientation, heat flux, inlet vapour quality and mass flux. Mingchen, et al. [35] experimentally showed that channel inclination and rotation of a heat sink operated with R134a at mass fluxes between 370 and 1250 kg/m^{2}s could significantly affect the heat transfer coefficient. They found that by heating a set of square horizontal parallel microchannels (0.5 mm in size) from below, rather than from above, the heat transfer coefficient could be 14% higher at low heat fluxes and 10% higher at high heat fluxes. Similar trends were also found by Li, et al. [20] for a non-uniformly heated microchannel with a width of 5 mm and depth of 0.5 mm at mass fluxes of 200 to 500 kg/m^{2}s, heat fluxes between 4 to 25 kW/m^2 for deionised water. They considered vertical upward and downward flows as well as horizontal flow with heating from above and below. They found that by heating the microchannels from below, the heat transfer coefficient was up to 20% higher than when heated from above, and that for upward flow, it was 25% higher than for downward flow. These influences were found to be magnified at low mass fluxes and high heat fluxes. At higher mass fluxes, orientation had less of an influence.

However, some studies have also been conducted indicating that channel orientation is not necessarily important. For instance, Ajith Krishnan, et al. [36] conducted a study with 31 parallel microchannels with a width of 305 μm, a depth of 290 μm, heat fluxes between 441 and 993 kW/m^2 and mass fluxes from 300 to 900 kg/m^{2}s with deionised water. They found that for these conditions, the channel's rotational position had little influence on the heat transfer performance of buoyancy-driven secondary flows. In another study, Ajith Krishnan, et al. [37] also experimentally considered flow-boiling in vertical upward and downward flows as well as horizontal flow with separate heating from above and below in a single microchannel (microgap) with a width of 20 mm and a height of 0.2 mm and mass fluxes of 303, 610 and 911 kg/m^{2}s. Again, it was found that channel orientation had little influence on the heat transfer coefficient. As before, this was attributed to the relatively high mass fluxes, which resulted in insignificant bubble-wall interactions.

Experimental measurement techniques, such as using thermocouple probes at specific locations underneath the heated surface to estimate the surface temperature distribution, are generally sufficient when quasi-steady-state time-averaged external characteristics are the focus of the investigation. However, the transient behaviour of the flow-boiling is much more challenging to capture experimentally and may require numerical simulations to gain better insight into the heat transfer process. Certain phenomena, such as the nucleation and departure of bubbles, occur over several milliseconds, which is smaller than the sampling frequency of most thermocouples [38] that are generally used in experimental studies. Flow velocity fields within the fluid are also challenging to obtain experimentally and temperature distribution within the fluid cannot be obtained.

Numerical modelling has been used as a tool to supplement our knowledge of the thermophysical characteristics of certain systems to visualise the inside of complex structures whose properties prohibit them from being properly analysed. For instance, in microchannels, the standard investigation methods coupled with small scales make visualising and quantifying the effects of the liquid layer thickness, the bubble dynamics and the spurious currents around the perimeter of bubbles difficult. While experimental studies can quantify the bulk properties, numerical studies are necessary to quantify the properties at a more localised level.

While numerical simulations do offer many benefits, the computational time that is required for small-scale transient simulations is significantly higher than for steady-state simulations. This inhibits many scenarios from being investigated and limits most researchers to two-dimensional axisymmetric models. Only a few three-dimensional studies have been conducted [39]. Such studies are also usually limited to the slug and annular two-phase flow regimes, with bubble nucleation and coalescence largely ignored due to their complexity.

A flow-boiling model has been developed to model heat transfer during slug flow as the elongated bubbles passed over a domain of interest [40]. The model divides the flow into three regimes with different heat transfer coefficients. The first is for a liquid slug passing through the domain of interest, the next is for an elongated bubble produced via evaporation, and the third is for a vapour slug. The model assumes that several bubbles will begin to nucleate on the microchannel wall. These bubbles stay in place after nucleation, growing until their radius reaches the walls of the channel. The bubbles then detach and join the flow in the axial direction. At this stage, the flow is in the slug regime, which involves the flow of alternating liquid and vapour regions that are described by the three-zone model.

Magnini, et al. [41] and Magnini, et al. [42] investigated the hydrodynamics and heat transfer characteristics of large vapour slugs in an axisymmetric domain, showing that the largest increases in heat transfer coefficient were obtained when the thickness of the liquid film between the slug and the wall was at its minimum, which usually occurred at the rear of the bubble. This increase was also felt in the wake of the bubble due to it interfering with the thermal boundary layer. This was built upon by Ferrari, et al. [43], who used the previous study as a base for a smaller three-dimensional model. The same scenario was investigated, that of large slugs flowing in a microchannel, except that this study looked at flow within a square channel. They found that when compared with circular channels, the vapour slug velocity was always higher, and that the minimum film thickness was lower due to fluid being drawn to the corners of the channels.

Due to the small length scales that occur when modelling flow boiling in microchannels, the effects of gravity are often deemed negligible, and therefore ignored. This is partly due to the prevalence of axisymmetric models, which restrict the use of gravity in all directions except when the gravitational vector is aligned with the axial direction. The effect of gravity on the thickness of the liquid film, which is largely regarded as the driving factor for increased heat transfer, has not been sufficiently investigated.

Several attempts to reduce the computational costs of flow-boiling simulations have been made by implementing adaptive mesh refinement models. Fondelli, et al. [44] used adaptive mesh refinement to recreate a dam break problem. They used a meshing method that refined cells that contacted an interface using the volume of fluid (VOF) method, which allowed them to recreate an experimental study in a three-dimensional domain. Mehdizadeh, et al. [45] also used adaptive

meshing to recreate a previous numerical investigation that involved slug flow in microchannels. With their technique, they were able to reproduce the results using 96% less cells. An adaptive mesh refinement model results in a reduction in computational cost for three-dimensional transient simulations.

Experimental studies on the effect of gravitational orientation on flow-boiling in microchannels have shown that the largest difference in local heat transfer coefficient between top- and bottom-heated channel occurs on the section of the heated surface that experiences bubble nucleation and departure [20, 46]. Numerical investigations into this phenomenon have shown that bubble departure during microchannel flow-boiling affects the heat transfer via the introduction of a liquid film between the vapour and the heated surface. Firstly, cooler liquid is brought into contact with the heated surface as the contact area between the bubble and the heated surface is reduced. This liquid then remains between the bubble and the heated surface, leaving a thin film that creates a large thermal gradient and therefore increases the heat transfer [47, 48].

Even though some attention has been given to channel inclination effects, few studies have investigated rotational effects experimentally, and none has been conducted in mini/micro channels with one-sided heating with a high aspect ratio at intermediary rotations. This is relevant to non-stationary electronic components and equipment that do not have a fixed gravitational orientation. These influences have not yet been investigated specifically for FC-72, which is a suitable fluid for electronic cooling. In addition, numerical investigations of flow-boiling have not investigated the phenomenon in three-dimensional high aspect ratio domains with one-sided heating at various rotations allowing the secondary flow behaviour to be captured.

The purpose of this study was to resolve this dearth of knowledge in the literature by producing heat transfer coefficient data for FC-72 in a single horizontal mini/micro channel with a high aspect ratio, heated on one side at intermediary rotations. In the two-phase region, rotational orientation, mass flux and heat flux were the variables investigated experimentally. Two- and three-dimensional numerical simulations were used to capture the secondary flows and to provide insight into heat transfer discrepancies between the various orientations that were investigated. In order to place emphasis only on the effect of channel rotation, and not on possible added complexities associated with flow mal-distribution, this study is conducted on a single channel only, instead of multiple parallel channels. Any rotational influences on the in-channel behaviour of a single channel, will also be present in multiple parallel channels.

2. EXPERIMENTAL SETUP

2.1 Test facility

Figure 1 offers a schematic representation of the experimental facility that was located at the University of Edinburgh. It enabled single-pass motion of FC-72 (C_6F_{14}), for heating and flow-boiling within an electrically heated min/micro channel test section at various rotational angle (θ) orientations.

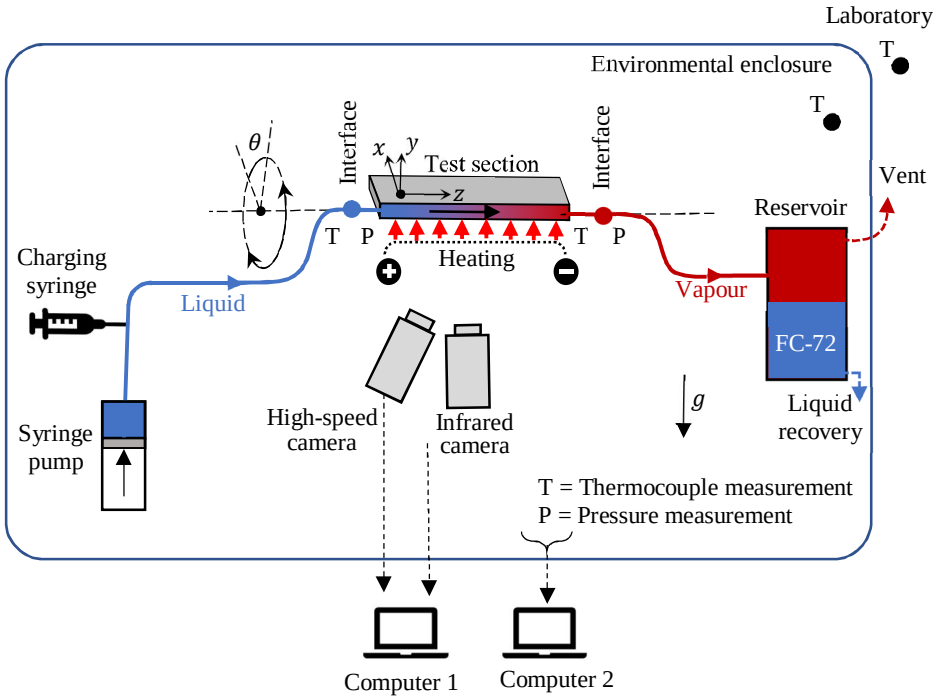

Figure 1: Schematic representation of the experimental setup

The same facility was used in a number of previous studies [15-17, 25-27, 49]. However, a few modifications were made to allow adjustment of the test section's inclination. The flow path consisted of (shown approximately from left to right in Figure 1): a syringe pump, a charging syringe, tubing and flexible hosing, an inlet interface to the test section (containing pressure and temperature sensors), a transparent test section, an outlet interface (also containing pressure and temperature sensors), flexible hosing, and a fluid collection reservoir. A high-speed camera and an infrared camera were used to enable flow visualisation and heated surface temperature observations. The flow path and the cameras were located within an acrylic glass enclosure to shield it from possible thermal variations in the laboratory.

The FC-72 was pushed through the flow path with a KDS 100 syringe piston pump with a 34.2 mm (± 0.02mm) internal diameter glass cylinder with a maximum enclosed volume of 100 ml. The piston was moved via a screw-thread mechanism connected to an electric motor. The motor speed could be adjusted to sustain a constant volumetric flow rate of between 0.1 μl/hour and 506 ml/hour with an accuracy of 1%. A suitably sized charging syringe was used to fill the system with fluid and to purge air from the passages.

The flexible tubing towards the test section inlet had a total length and internal diameter of approximately 500 mm and 3 mm respectively, followed by a short length of rigid tubing with a length and internal diameter of 20 mm and 5 mm respectively.

Interface with the test section (at its inlet and outlet) was achieved via two identical assemblies consisting each of a mounting block, and T-type and L-type push-pull PEM0310W John Guest® fittings (see Figure 2). An Omega® PXM219 gauge pressure transducer [50] with a response time of approximately 2 ms, a measuring range of 0 to 250 kPa and an accuracy of 0.025% of the full scale was connected to the flow path via the T- fitting. A K-type thermocouple with a

measuring tip of approximately 1 mm was located directly in the fluid. The thermocouple leads passed through a small hole at the L-fitting, which was resealed with Araldite® Rapid epoxy.

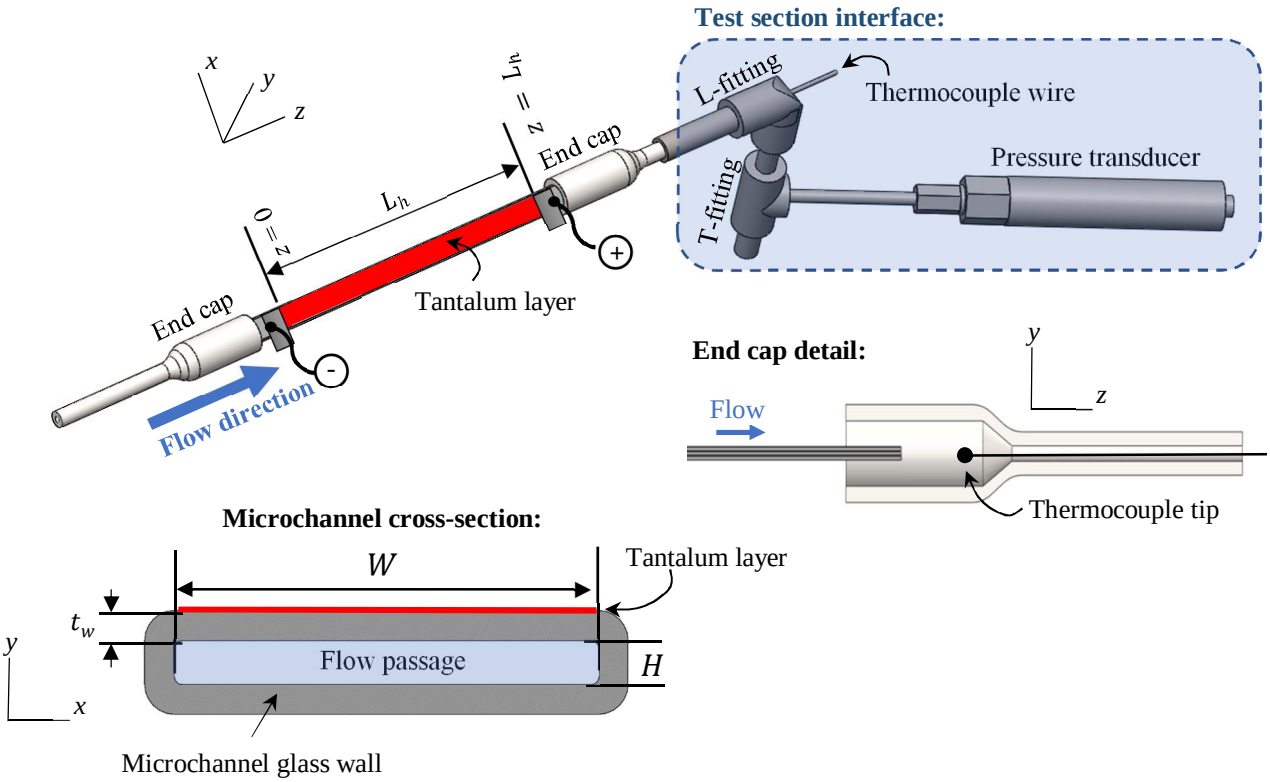

Figure 2: Tantalum-coated test section with its system interface assembly

The orientation system consisted of a side-mounted Axminster® rotary table and an aluminium frame onto which the inlet and outlet interface assemblies were bolted. The inclination of the channel (which was kept horizontal during test-runs in this study) could be adjusted via the rotary table, while the rotation of the test section could be modified by simultaneously adjusting the angular position of the L-type push-pull fittings at the inlet and outlet interface assemblies.

The test section (described in more detail later) was relatively flat with glass walls and the test section experienced one-sided electric heating via a transparent metal coating.

A glass reservoir with a volume of approximately 350 ml was used to collect the FC-72 from the outlet of the test section via a combination of flexible hosing and rigid tubing, similar to that at the inlet. The tubing, hosing and the reservoir were not thermally insulated and resulted in the condensation and cooling of the FC-72 into liquid form. The reservoir also had a drain to recover the liquid and a vent to the outside of the laboratory to maintain the system at atmospheric pressure (approximately 100 kPa).

A Basler® acA800-510um CCD high-speed camera with a 12 mm fixed lens, a resolution of 800 x 600 pixels, and a maximum frame rate of 511 frames per second (fps) was used to record the flow visualisations inside the test section. The

camera position was altered according to the test section orientation and always viewed the channel from the heated wall side, with a backlight located at the opposite side of the channel.

A FLIR® A645 infrared camera with a thermal sensitivity of 20 mK, a resolution of 640 x 480 pixels, and a maximum frame rate of 25 fps was used to record the external surface temperature of the heated wall of the test section. Care was taken with its viewing angle to prevent self-generated heat reflection aberrations by orientating the camera at a slight orthogonal offset of less than 5° relative to the test section surface.

As mentioned, the flow path and the cameras were housed in an acrylic glass enclosure. It measured 1 m x 1 m x 1 m and its internal temperature was monitored and recorded by a K-type thermocouple. Another K-type thermocouple was used to monitor and record the ambient laboratory temperature.

The test section was electrically heated by a dial operated Clairtronic® 240V alternating current VARIAC transformer connected to a direct current (DC) rectifier. The DC supply current and voltage were measured with two MASTECH® MS8239 multimeters, which had measuring accuracies of 1%+10 for the current (mA) and 0.5%+2 for the voltage (V) readings. The resolution of the current reading was to two decimal places and the voltage reading was to one decimal place.

Data acquisition occurred via two computers. One computer was connected to the infrared and high-speed cameras, while the other was used to log the thermocouple and pressure transducer data via a National Instrument® SCXI-100 chassis with a SCX1-1303 data card for thermocouple readings and a National Instrument USB-6008 stand-alone data acquisition unit for pressure transducer readings. The latter had a time delay in readings from different channels of approximately 200 µs.

Test section

Figure 2 also gives a schematic representation of the test section design in orthographic view and cross-sectional view. The test section consisted of a hollow inlet circular borosilicate glass end cap, a rectangular extruded borosilicate glass channel, and another hollow borosilicate glass end cap at the outlet.

Due to possible breakage, a set of identical channels were procured from VirtoCom™. Each had an axial length (L) of 100 mm ± 0.02 mm in the z direction, an inner width (W) of 5 mm ± 0.02 mm in the x direction, and an inner channel height (H) of 0.5 mm ±0.02 mm in the y direction. The wall width (t_w = 0.35 mm ± 0.02 mm) was uniform along the length of the microchannel. The flow passage had a hydraulic diameter (d_h) of 909 µm and its channel aspect ratio was 10. A portion of the length was electrically heated (L_h = 75 to 80 mm ± 0.02 mm) via an electric current that was passed through a tantalum (Ta) metal layer, which was sputtered on one of the external surfaces of the channel.

Classification of the channel as a micro/mini channel was done using the confinement number ($Co = 0.797$), capillary length ($L_{cap} \approx 724\,\mu m$) and the bond number ($Bd \approx 1.58$), all indicating that microscale physics would dominate the bubble interactions in the channel. It is important to note that the surface tension of FC-72 was low when compared with fluids like ethanol and water, which influenced the magnitude of the non-dimensional numbers.

The glass channels were prepared by first cleaning them in a sulfuric acid and hydrogen peroxide solution for 30 minutes to remove impurities and biological agents from all surfaces; then by flushing them with deionised water; then by drying them at an elevated temperature; and finally, by sputtering a 22.5 nm thick layer of tantalum onto one of the channel's sides. The sputtering process occurred simultaneously for all channels and were done in a Class 10 cleanroom at the Scottish Microelectronics Centre by using an Oxford Instruments® Plasmalab System400. The thin layer of tantalum was transparent in the visible spectrum allowing for flow visualisation and had a typical electrical resistance of 3.75 kΩ over the heating length.

The end caps were produced by a glass blower and placed at both ends of the microchannel. The large diameter side of each end cap had an inner diameter of 6 mm and was approximately 30 mm long, while the smaller diameter side had an inner diameter of 3 mm and was also approximately 30 mm long (see Figure 2). The end caps were joined to the microchannel using Araldite® Rapid epoxy, which produced airtight seals. The epoxy had a melting temperature of 80 °C and did not react with FC-72.

Electric terminals consisting of carefully placed strips of aluminium foil were tightly wrapped around the channel, held firm and were connected to the DC rectifier.

3. EXPERIMENTAL PROCEDURE

3.1 Calibration

Before the main tests were conducted, the temperature and pressure probes were calibrated. The thermocouples were calibrated with an OPTIMA® T100 thermal water bath, which had a temperature measurement uncertainty of ± 0.1 °C. Calibrations were conducted during steady-state isothermal conditions between 0 °C and 60 °C at intervals of 5 °C. For each calibration target temperature, 5 minutes were allowed for the water bath to reach thermal equilibrium. This was followed by data recording over a period of 15 seconds at 100 Hz, before the bath was adjusted to the next target temperature. Calibrations were repeated at different periods (before and after the main experimental test period) to check for possible drift in thermocouple output. No observable drift was present and the same calibration correction factors employed throughout the investigation.

Calibration of the pressure transducers was done with a SPER SCEINEFITIFC® Model 84083 manometer. Each pressure transducer was connected to the manometer with a gas tube after which a hand-operated pump was used to increase the pressure in the tube. Once the pressure measurement on the device was stable, the output measurement from the pressure transducer was recorded. Both pressure transducers were calibrated *in situ* within the enclosure at their intended operating orientation.

The emissivity of the tantalum-sputtered surface, which was needed as a setting on the infrared camera, was determined by using a technique described by Madding [51]. Infrared temperature measurements were taken under controlled conditions at two steady-state temperature conditions (of approximately 16 °C and 35 °C) on the tantalum surface, as well as on a reference surface with a known emissivity. Correct temperatures of both surfaces were obtained via calibrated K-type thermocouples, which were carefully installed onto the surfaces. By comparing the infrared camera

readings with the measured thermocouple temperatures, the emissivity of both surfaces was determined. The calculated emissivity for the reference surface was used to validate the method. The emissivity of the tantalum surface was found to be 0.8 (with an accuracy of 11%), which agreed well with the emissivity reported previously for the same type set-up [25, 28, 49]. The uncertainty was high due to infrared camera uncertainty in the temperature measurement. The other infrared settings, which included the infrared camera lens temperature, atmospheric temperature and reflected temperature, were assumed to be uniform and were obtained from the steady-state thermocouple measurement taken inside the acrylic glass enclosure (mentioned earlier).

Even though the KDS 100 syringe pump was factory calibrated, its digital display volumetric flow rate setting was manually checked at 50, 100 and 200 ml/h, which was representative of the volumetric flow rates used in the experiments. Pumped fluid was collected, independently measured and compared with the target setting, which was found to be correct.

3.2 Test matrix

The literature indicates that lower mass flux conditions are more susceptible to buoyancy-driven influences. Therefore, in this study, mass fluxes (G) of 10, 20 and 40 kg/m^{2}s were considered in horizontal microchannels. The rotational orientation of the channel (about the z-axis) is shown in Figure 3 and was defined by θ which was measured from the horizontal plane. For each mass flux, seven rotational angles were tested ranging from 0° (heating from below, with the tantalum surface being horizontal) to 180° (heating from above, with the tantalum surface being horizontal), at intervals of 30° (± 1°).

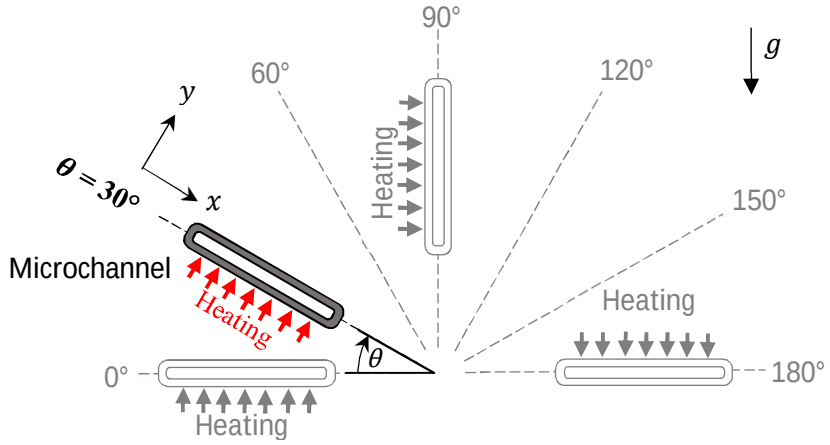

Figure 3: Rotational positions of the channel at various testing positions

The subcooled liquid inlet temperature (T_{in}) ranged between 16 °C and 23 °C depending on the temperature of the laboratory and was constant during each test case. The saturation temperature (T_{sat}) was 56 °C (± 0.14 °C), which was directly linked to the atmospheric operating pressure within the flow path.

Different associated applied heat rates were used for each mass flux. This was to ensure the onset of nucleate boiling within the test section, to prevent dry-out within the channel and to ensure the tantalum surface temperatures were below 150 °C. The latter was a restriction imposed by the ability of the infrared camera. At 10 kg/m^{2}s, a heat input range of 1.19

to 2.76 W was used; at 20 kg/m^{2}s, a heat input range of 1.96 to 5.23 W was used; while at 40 kg/m^{2}s, a heat input range of 3.73 to 6.09 W was used. These heating rates produced different in-channel heat flux values as described later.

3.3 Experimental method

Before each main set of tests was conducted, the flow path (which included a test section) was flushed several times with deionised water at a volumetric flow rate of approximately 10 L/s to remove traces of dust and impurities. High-pressure air was then passed through the flow path for at least 30 minutes, and the acrylic glass enclosure, which was equipped with an electric heating element, was heated to 36 °C for 5 minutes to ensure full evaporation and removal of the water.

To prevent the presence of air bubbles during tests, the syringe pump was preliminarily charged with pre-used FC-72 and the flow path was flushed again. This was done while slowly altering the channel inclination from horizontal flow to vertical upward flow, then to vertical downward flow, and back to horizontal flow, at least three times until from inspection the test section and all upstream and downstream tubing were purged of air, and the syringe pump cylinder was empty. The syringe pump was then refilled with virgin FC-72 and the remaining flow path was re-flushed by means of the charging syringe.

The channel inclination and rotation positions were set by adjusting the orientation system. Care was taken with the orientation of the pressure transducers to match their layouts with the geometric conditions when they were calibrated. The infrared and high-speed camera positions were adjusted and clamped. The position of the high-speed camera relative to the test section and the backlight required meticulous adjustment, while care was taken to prevent self-reflection by the infrared camera.

Because it was not possible to thermally insulate the test section, significant heat loss from the tantalum surface to the acrylic glass enclosure occurred during the flow-boiling experiments. In order to later obtain the local and average heat transfer coefficients, it was important to be able to determine the test section heat transfer rate into the fluid. However, during flow-boiling conditions, it was generally quite challenging to accurately and directly determine the inlet and outlet thermodynamic states of the fluid based on the measured pressure and temperature values at the inlet and outlet of the test section. Therefore, it would be impossible to calculate the heat transfer rate based on these inlet and outlet measurements. Alternatively, if the heat loss rate from the tantalum to the surroundings could be determined, the heat loss could later be subtracted from the total power input to the heating layer, which would ultimately enable determining the relevant heat transfer coefficients.

In order to find the heat loss characteristic of each test section orientation, single-phase liquid experiments had to be performed first. For the liquid flow conditions, the total heat input, the heat absorbed by the fluid (based on the temperature rise of the fluid in the test section), the tantalum surface temperature as obtained from the infrared camera, and the surrounding temperature in the acrylic glass enclosure was obtained relatively easily. As discussed later, this enabled the characterisation of the heat loss rate from the heated tantalum surface as a function of the temperature difference between the tantalum and the surrounding air. For this purpose, five steady-state single-phase tests were conducted for each test

section orientation at mass fluxes of G = 10, 20 and 40 kg/m^{2}s, and at a range of applied heat fluxes. This resulted in scenarios which produced a range of temperature differences between the tantalum and its surrounding. To reduce experimental uncertainty, the single-phase tests were conducted such that the temperature increase of the fluid over the test section was at least 5 °C. In these tests, steady state was defined when the outlet temperature changed by less than 0.1 °C over 3 minutes.

Once enough single-phase data was collected, the main two-phase flow-boiling tests commenced. The syringe pump settings were adjusted, and the pump was started. The power input to the tantalum layer remained off until fluid was seen collecting in the reservoir at the outlet of the set-up. The heating was gradually increased to just below saturation conditions to prevent sudden and unexpected system instability, which could result in damage to the test section. Heat input was slowly increased to the target value until a relatively stationary nucleation point was present at a suitable location in the channel.

Accurate capturing of the flow behaviour was only possible during quasi-steady-state flows, which were defined when the outlet temperature remained constant within a variation of less than 0.2 °C over a period of 3 minutes, the nucleation site remained fixed and the perceived flow pattern remained consistent or periodic in nature. After an additional 3 minutes of steady conditions, the pressure transducer and thermocouple data were logged at 100 Hz for a period of 60 seconds per experiment and approximately 7 minutes per heat flux. High-speed camera footage was recorded at between 100 and 140 fps depending on the flow pattern behaviour for a period of 70 seconds spanning from before the infrared image started to record until after the infrared images stopped recording. The infrared footage was recorded at 25 fps for a period of 60 seconds. The input power and volumetric flow settings were recorded manually. Care was taken to ensure time synchronisation between the two computers as well as the cameras.

Each test case and heat flux condition were repeated three times, before the next heat flux and/or mass flux and/or rotational orientation case was considered. At the end of each experimental set, the collected FC-72 in the outlet reservoir was retrieved and stored in a sealed glass jar until it could be disposed of safely.

4. DATA REDUCTION

Because the data acquisition systems and cameras were operated at different logging frequencies and frame rates, relevant time synchronisation was required, which was done with MATLAB. Time averaging of data was done in the calculation of the heat transfer coefficient including inlet temperature, outlet temperature and surface temperature.

4.1 Characterisation of the heat loss

As mentioned, diabatic steady-state single-phase liquid experiments were conducted to characterise the heat loss behaviour from the tantalum surface to the surroundings. First, the absorbed heat into the fluid ($\dot{Q}$) was determined from the change of temperature of the fluid:

$$\dot{Q} = \dot{m} c_p (T_{out} - T_{in}) \quad (1)$$

where $\dot{m}$ is the mass flow rate of the FC-72, c_p is the specific heat capacity of the fluid, and T_{out} and T_{in} are respectively the time-averaged outlet and inlet fluid temperatures obtained from the relevant outlet and inlet thermocouples. The mass flow rate was calculated from the syringe pump volumetric flow rate ($\dot{V}$) and the fluid density (ρ):

$$\dot{m} = \dot{V}\rho \tag{2}$$

The specific volume and density values were assumed to be constant and were calculated from correlations supplied by the fluid manufacturer [5], at the thermocouple temperature measurement inside the interior of the acrylic glass enclosure (T_0):

$$c_p = 1010 + 1.554T_0 \tag{3}$$

$$\rho_{liquid} = 1740 - 2.61T_0 \tag{4}$$

The heat loss ($\dot{Q}_0$), from the tantalum surface was calculated by taking the difference between the power input to the heating layer ($\dot{Q}_h$) and the absorbed heat into the fluid:

$$\dot{Q}_0 = \dot{Q}_h - \dot{Q} \tag{5}$$

where the power input was determined from the measured DC voltage (U) and current (I) applied to the tantalum layer:

$$\dot{Q}_h = U \cdot I \tag{6}$$

The difference in temperature between the warm tantalum layer and the surrounding air was calculated:

$$\Delta T_0 = \bar{T}_h - T_0 \tag{7}$$

where ($\bar{T}_h$) is the spatially average tantalum surface temperature obtained from the infrared measurements.

After the heat loss rates and temperature differences were calculated for each test case, the heat loss was expressed as function of ΔT_0 via a power curve:

$$\dot{Q}_{0,\Delta T_0} = a\Delta T_0^b \tag{8}$$

where a and b are constant values which were determined from the data.

This resulted in 21 heat loss equations, one for each channel rotational position and mass flux. The equations correlated the heat loss within ± 1.49% (± 0.1W) for the measured ΔT_0 values ranging from 5 to 50 °C. In the subsequent flow-boiling experimental data, significantly higher ΔT_0 values were present, ranging from 5 to 130 °C, due to the increased heat flux that was needed to sustain flow-boiling. Due to the nature of convection, which was the dominant heat

loss mechanism, it was assumed that the heat loss equations were also applicable to the elevated temperature operating conditions.

4.2 Heat transfer coefficient

The local heat transfer coefficient, which depended on the axial coordinate (z), was calculated as follows:

$$\alpha(z) = \frac{\dot{q}}{T_{w,z} - T_{b,z}} \tag{9}$$

where $\dot{q}$ is the effective heat flux after heat losses were taken into consideration, $T_{w,z}$ is the local internal heated wetted wall temperature and $T_{b,z}$ is the local bulk fluid temperature.

The heat flux was assumed uniform along the test section length and was based on the nett absorbed heat into the fluid and the internal heated side surface area, calculated from L_h and W (both measured by a Vernier Calliper in the installed state of the microchannel):

$$\dot{q} = \frac{\dot{Q}_h - \dot{Q}_{0,\Delta T_0}}{L_h W} \tag{10}$$

Here, $\dot{Q}_h$ was calculated from equation (6) and $\dot{Q}_{0,\Delta T_0}$ was calculated with the relevant version of equation (8) based on the actual value of ΔT_0 via equation (7).

$T_{w,z}$ and $T_{b,z}$ were calculated by considering control volumes of equal size along the heated length. Each control volume had a width of W and an axial length equal to size represented by one pixel on the infrared camera images. As such, the number of control volumes and their axial direction sizes depended on the actual heated length of test section, the resolution setting on the infrared camera and the relative placement of the camera to the test section (distance from the test section). In general, there were approximately 400 pixels along the heated length and 25 pixels across the width of the channel.

Due to the small distance between the inner wetted surface of the microchannel and the heated external surface, the temperature difference across the wall thickness was neglected and it was assumed that the local inner-wall temperature was equal to the local external heated wall temperature: $T_{w,z} = T_{h,z}$. This assumption was supported by low Biot numbers (less than 1) ranging from 0.06 to 0.61 in this study. Thus, $T_{w,z}$ was determined via MATLAB as the arithmetic average of the infrared camera pixel temperature values for each control volume.

Calculating the local bulk fluid temperature was slightly more complicated (specifically during flow-boiling) and was based on the thermodynamic properties of FC-72, the heat input per control volume, and the mass flow rate. Due to the macroscopic nature of thermodynamic calculations, the obtained local bulk fluid temperatures (one each per control volume) represented the thermodynamic average temperature of the fluid, and not the temperature at molecular level.

Because the FC-72 entered the test section as a subcooled liquid, there was a region where the fluid experienced sensible heating in its liquid phase, which is characterised by an increase in the fluid temperature. However, once bulk (averaged) saturation conditions were reached, the temperature remained constant at its saturation level (approximately 56 °C in this study).

MATLAB was used to calculate the local bulk fluid temperature by using the following relationships, where z = 0 at the start of the heated length.

If in the liquid phase ($T_{b,z} < T_{sat}$):

$$T_{b,z} = T_{in} + \frac{\dot{q}Wz}{\dot{m}c_p} \tag{11}$$

If in the two-phase region:

$$T_{b,z} = T_{sat} \tag{12}$$

T_{sat} was determined by using the time-averaged outlet temperature measure by the thermocouple and cross-checked with the expected thermodynamic saturation temperature at atmospheric pressure.

4.3 Local vapour quality

The local vapour quality (χ_Z) at location z was determined by applying the energy balance principle:

$$\dot{q}(zW) = \dot{m}c_p(T_{sat} - T_{in}) + \dot{m}h_{fg}\chi_z \tag{13}$$

which can be rewritten as:

$$\chi_z = \frac{\frac{\dot{q}_z W}{\dot{m}} - c_p(T_{sat} - T_{in})}{h_{fg}} \tag{14}$$

Here, $\dot{q}$ is defined by equation (10) and h_{fg} is the latent specific heat of evaporation, which was obtained from the fluid manufacturer [5] to be 88 kJ/kg.

4.4 Total pressure difference

The total pressure difference was calculated using the inlet (P_{inlet}) and outlet pressure (P_{outlet}) readings at each time step which were then average in time.

$$\Delta P = P_{outlet} - P_{inlet} \tag{15}$$

The outlet pressure was used as the reference as it resulted in most values producing positive results.

4.5 Uncertainty analysis

The uncertainties of some important input parameters and calculated quantities are summarised in Table 1. Uncertainty propagation calculations were done by using the method by Moffat [52]. This method defines variables to have either absolute or relative uncertainties. Absolute errors were determined by considering the bias and random errors in the readings with the uncertainty presented as a specific value at all input ranges. Relative uncertainties were scaled based on the parameter input range using the relative error of other uncertainty parameters to determine the percentage error of a parameter.

Table 1: Absolute uncertainties of the input parameters

Parameter	Maximum relative error	Minimum absolute error
Thermocouple temperature (T)		± 0.14 °C
Saturation temperature (T_{sat})		± 0.14 °C
Infrared camera temperature (T_w, T_h)		± 2 °C
Heat absorbed (Q)		± 0.16 W
Channel length (L)		± 0.02 mm
Channel internal width (W_{in})		± 0.02 mm
Channel internal height (H_{in})		± 0.02 mm
Local distance from inlet (z_l)		± 0.09 mm
Rotational orientation (α)		± 1°
Liquid density (ρ_{liquid})		± 0.37 kg/m^3
Pressure Drop (ΔP)		± 141 Pa
Voltage (U)	0.5%+2 (at resolution)	2.68 V
Current (I)	1%+10 (at resolution)	1.75 mA
Heat flux ($\dot{q}$)	4.7%	0.13 kW/m^2
Heat transfer coefficient (α)	4.7%	60 W/m^{2}K
Volumetric flow rate ($\dot{V}$)	1%	2 ml/hr
Mass flux (G)	0.41%	0.16 kg/m^{2}s
Vapour quality (χ)	4.7%	0.05

The random uncertainty is represented either as σ which is the relative uncertainty represented with a % or as ϵ which is the absolute error and has the same units as the measurement. Absolute uncertainties were calculated with the absolute uncertainty of the components. For example, the uncertainty of the pressure drop was the squared root mean of the inlet and outlet pressure as shown in equation 16.

$$\epsilon_{\Delta P} = \sqrt{\epsilon_{P_{inlet}}^2 + \epsilon_{P_{outlet}}^2} \tag{16}$$

While the relative uncertainty of a variable was calculated using the relative components of the various components. For instance, the heat flux was the squared root mean of the heat absorbed by the channel and the relative uncertainty of the heated area as shown in equation 17.

$$\sigma_{\dot{q}} = \sqrt{\sigma_{Q_{ab}}^2 + \sigma_{A_{heated}}^2} \tag{17}$$

The methods described in equation 16 and 17 were employed for all parameters depending on whether a quantity had an absolute or relative uncertainty.

5. EXPERIMENTAL RESULTS

5.1 Validation

The experimental method was validated against the results of Wang, et al. [15], who also conducted work on FC-72. For comparison purposes, a channel, which was prepared in the same way as discussed earlier, but with an internal width of 6 mm and height of 3 mm respectively, was used. A mass flux of 44 kg/m^{2}s and θ = 0° was considered with an effective heat flux of $\dot{q}$ = 6.5 to 10 kW/m^2. Figure 4 shows a comparison of the arithmetic average heat transfer coefficient in the two-phase region with the results of Wang, et al. [15]. This heat transfer coefficient was averaged in time and spatially over the entire two-phase region. Inlet temperatures were time averaged. Also shown in the figure are the uncertainty values of both data series. As a result of this agreement, the facility was determined to be correctly validated.

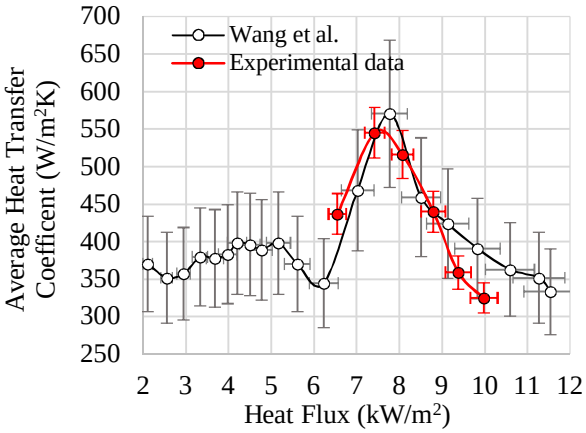

Figure 4: Experimental validation of experimental facility with literature Wang, et al. [15]

5.2 Flow patterns

The flow behaviour in the two-phase region of the channel was defined by several defining bubble behaviours. In all the flow-boiling cases, the following regions were observed from the flow visualisation footage obtained from the high-speed camera: single-phase liquid flow where the fluid experienced sensible heating, flow-boiling nucleation and bubble formation and bubble growth into vapour slugs towards the outlet. It was found that axial location of the nucleation site was dependent on the mass flux and heat flux combinations. For instance, the nucleation site moved closer to the inlet when heat flux was increased or when the mass flux decreased. However, there were significant differences in the bubble behaviour during the bubble growth stages depending on θ and whether the bubbles detached. These differences are

illustrated in Figure 5, which shows arbitrary selected cases at θ = 0°, 90° and 180° at a mass flux of 40 kg/m^{2}s and heat flux of 14 kW/m^2.

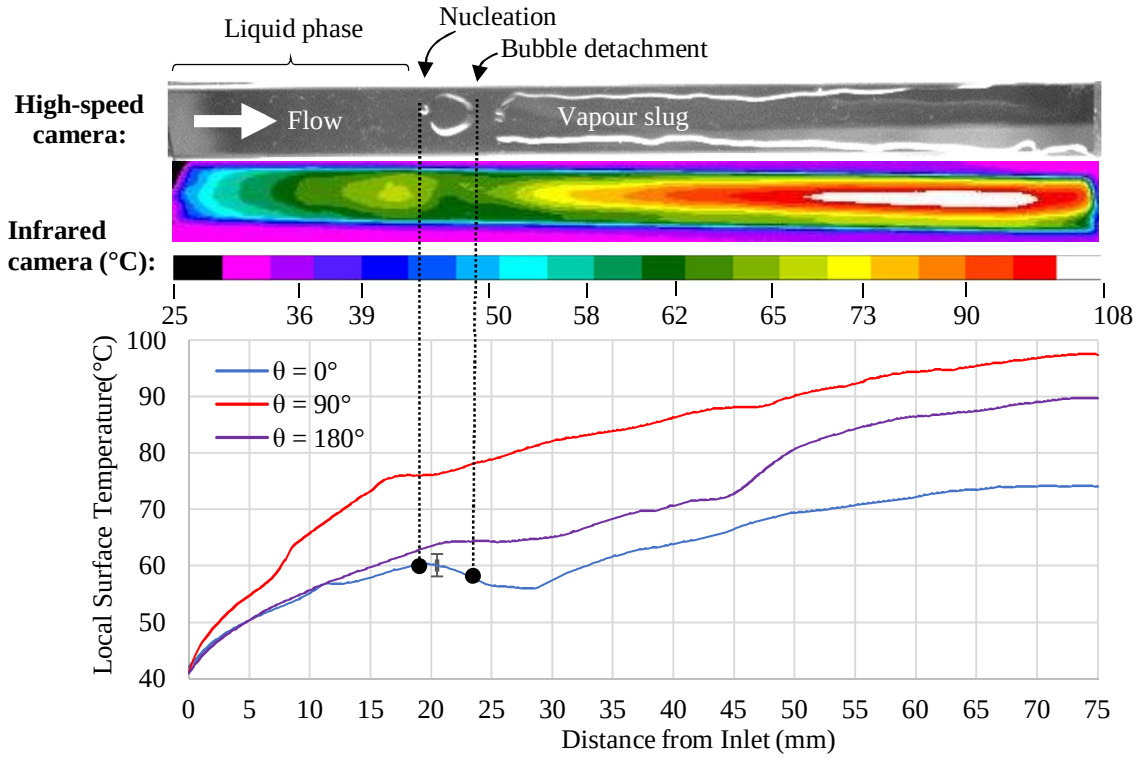

Figure 5: Flow pattern, infrared map, and local surface temperature plots for θ = 0° at a mass flux of 40 kg/m^{2}s and a wetted heat flux of 14 kW/m^2, compared with surface temperatures plots for θ = 90° and 180°

The figure contains a snapshot of the governing flow pattern captured by the high-speed camera and an infrared camera image for θ = 0° (heating occurring from below), as well as the time-averaged heated wall temperature profile along the channel length. For comparison purposes, the figure also shows the local wall temperatures for θ = 90° and θ = 180°. Based on the flow visualisation, initially, the flow was in single-phase with no bubbles visible. Along the channel, as the total absorbed heat into the fluid increased, as seen on both the surface temperature plot and the infrared image of the channel, a hot spot is shown just prior to nucleation. On the flow visualisation, this position is seen at approximately the point of bubble nucleation and is labelled in the figure. At this point, the surface temperature reached a local maximum, followed towards the right by a region of bubble growth until the bubble reached a large enough volume to detach from the surface. Once the bubble detached from the surface, a local low surface temperature is observed. Along the flow path, the bubble enlarged further and became confined, decreasing the liquid film thickness in contact with the heated wetted perimeter until dry-out conditions occurred. This increased the surface temperature and decreased the heat transfer performance (as will be shown later). Even though the mass flux and heat flux were the same as with the θ = 0° case, for θ = 90° and 180°, no clear bubble detachment was observed (flow visualisation not included in the figure), which resulted in significantly warmer surface temperatures, as seen in the temperature plot. In these cases, the surface temperatures continued to increase steadily and there was no localised decrease in the heated surface temperature – indicating the absence of bubble detachment.

In addition to the difference in the axial wall temperature profiles, other differences in the bubble behaviour were also noticed for θ = 0° and θ = 180° (when the heated surface was horizontal). For θ = 0° and θ = 180° nucleation sites were in the centre of the channel and symmetric thermal gradients in the x direction about the centre line were observed. However, for rotated cases with θ = 30°, 60°, 90°, 120° and 150°, the nucleation sites were in the highest position in the channel, away from the centre line.

In general, bubble detachment from the nucleation site took one of two forms. The first was when the bubble moved off the heated surface with motion in both the flow direction and perpendicular to the flow direction forcing colder fluid onto the surface, θ = 0° (discussed in more detail later). The second was where the bubble slid on the surface away from the nucleation site and formed a column of fluid from the nucleation site into the large vapour slug that always formed, θ = 30°, 60°, 90°, 120° and 150°. The θ = 180° case had bubbles slide from the nucleation site in contact with the heated wall similar to cases with θ = 30°, 60°, 90°, 120° and 150°, but with bubbles detaching from the heated surface like θ = 0°. The location of the nucleation site also had an impact on the magnitude of the effect of the bubble detachment. In the θ = 30° cases, a second nucleation site was present at the bottom of the channel closest to the ground giving the bubble a large vertical distance to travel producing a significant impact on the heat transfer.

Based on the experimental data, the bubble-settling location after departure from the nucleation site can broadly be grouped into two types: where the heated surface was horizontal (θ = 0° and θ = 180°) and where the heated surface was not horizontal (θ = 30°, 60°, 90°, 120°, 150°). By rotating the channel, the bubble's buoyancy allowed the vapour to move to the side of the channel. This motion forced the bubble to become confined in the cross-section of the channel at a faster rate which produced dry-out on the upper side of the channel.

Cross-sectional temperatures were affected by the location of the nucleation sites as well as the location where a bubble settled. As mentioned, the horizontal channel cases (θ = 0° and 180°) had nucleation sites on the centre of the channel, which resulted in bubble detachment from the heated surface and bubble confinement on the entire cross-sectional width of the channel due to an even distribution. Non-horizontal channel cases (θ = 30°, 60°, 90°, 120°, 150°) had a cross-sectional temperature gradient that was much larger because the vapour settled at the top of the channel with liquid underneath.

5.3 Local heat transfer coefficients

In Figure 6 the time-averaged local heat transfer coefficients for the rotational orientations θ = 0°, 30°, 60°, 90° and 180° are plotted along the flow direction at various vapour qualities with a heat flux of $\dot{q}$ = 8 kW/m^2 and a mass flux of G = 20 kg/m^{2}s. Note that the vapour quality increased along the axial direction, and that the vapour quality in this figure is also an indication of the relative axial location along the channel. Negative vapour qualities represent single-phase liquid states.

It can be seen that from the inlet, while the fluid was still in the liquid phase, there was a general decrease in the heat transfer coefficient because of thermal flow development during sensible heating. The heat transfer coefficient increased as the flow neared nucleation for θ = 0° but remained constant for all other rotations. At the point of nucleation, a local

maximum in the heat transfer coefficient was present for θ = 0°. After bubble departure, the heat transfer coefficient of the θ = 0° case reached its ultimate maximum value after which it rapidly declined. Non-horizontal flows did not have bubble detachment and thus did not have local peaks in the heat transfer coefficient. Once the vapour slugs had formed, the heat transfer coefficients of all rotations reached similar constant values.

The relatively large spread in the heat transfer coefficient values in the single-phase section was due to flow reversals (which depended on the heat flux and mass flux) in the two-phase region of the channel. As such, the upstream single-phase portions never experience steady state or fully developed flow conditions. The single-phase region data that resulted in the highest local heat transfer coefficients, agreed with the cases where flow reversal (partial or full) was more prevalent. Such flow reversals were recorded by the flow visualisation camera.

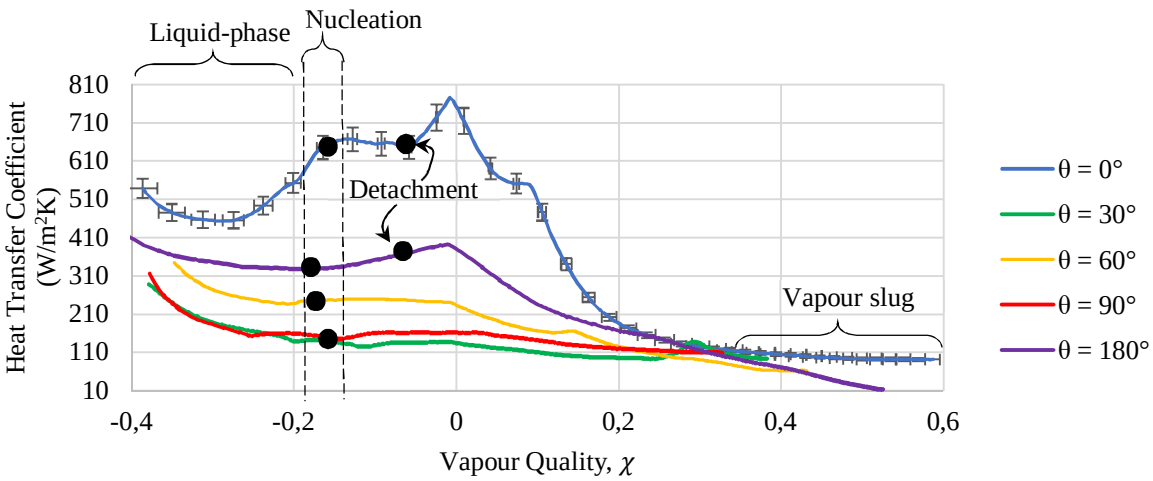

Figure 6: Local heat transfer coefficient for θ = 0°, 30°, 60°, 90° and 180° at a mass flux of 10 kg/m^{2}s and a heat flux of 12.5 kW/m^2

Figure 7, Figure 8 and Figure 9 compare the influence of θ on the time-averaged local heat transfer coefficient at chosen vapour qualities from 0 to 0.25. Each figure gives the results at a different mass flux (G = 10, 20 and 40 kg/m^{2}s) and a different effective heat flux, determined via equation (10) ($\dot{q} \approx$ 4.5, 8 and 12 kW/m^2) respectively.

The single-phase region also presents interesting results with an initially decline in the heat transfer coefficient which in the cases of 30°, 60° and 90° remains constant leading up to the point of nucleation. However, for 0° and 180° an increase in the single-phase heat transfer coefficient was observed before nucleation with a more pronounced increase experienced for 0°. It is posited that due to the conservation of mass and the decrease in density of the fluid as it is heated and undergoes vaporization, there would be an increase in the velocity.

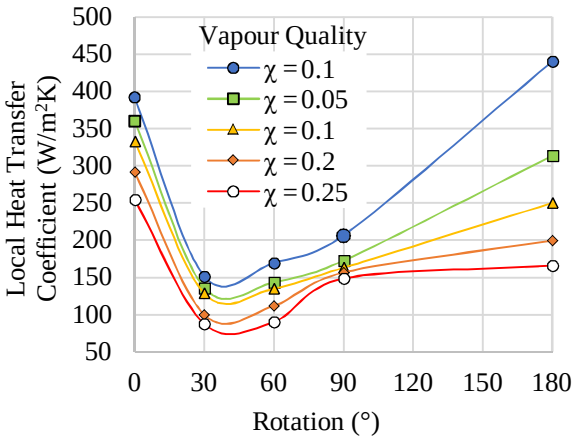

Figure 7: Local heat transfer coefficients in terms of θ at a mass flux of 10 kg/m^{2}s, a heat flux of 4.5 kW/m^2, at qualities of χ = 0, 0.05, 0.1, 0.15 and 0.2

Figure 7 shows that for 10 kg/m^{2}s, both θ as well as the vapour quality had a significant influence on the heat transfer coefficient. The highest heat transfer coefficients were obtained at θ = 0° and 180°, and the lowest heat transfer coefficients were achieved between θ = 30° and 60°. The best heat transfer coefficients (irrespective of the channel rotation) were achieved at a vapour quality of zero, which coincided with the occurrence of nucleation. For all angular cases, the heat transfer coefficient decreased as the vapour quality increased. For this particular mass flux and heat flux, the highest heat transfer coefficient of 440 W/m^{2}K was recorded for a top-heated case (θ = 180°) at the nucleation site. For the bottom-heated case (θ = 0°), the nucleation site exhibited a heat transfer coefficient of 390 W/m^{2}K, which was approximately 11% less than for the top-heated case. The worst-performing case (θ = 30°) exhibited a nucleation site heat transfer coefficient that was 66% lower than for the top-heated case. However, for all the other vapour qualities included in the figure, the bottom-heated case outperformed the top-heated case. For instance, at vapour qualities of χ = 0.1 and 0.2, the bottom-heated case produced heat transfer coefficients that were 33% and 50% higher than for the top-heated case respectively.

In Figure 8, for a mass flux of 20 kg/m^{2}s and an effective heat flux of approximately 8 kW/m^2, a different behavioural trend can be observed. The best heat transfer coefficients were still recorded at the nucleation site (χ = 0), and the heat transfer coefficient still decreased with vapour quality (except for one data point at θ = 30° as discussed in a next section). However, for this mass flux and heat flux combination, bottom heating significantly and consistently outperformed the other rotational orientations. For instance, at vapour qualities of χ = 0, 0.1 and 0.2, bottom heating resulted in heat transfer coefficients that were 100%, 132% and 134% greater than for top heating. As before, based on the data, the worst-performing cases were at approximately θ = 30°, which exhibited heat transfer coefficients that were between 60% and 81% lower than for θ = 0°. The mentioned anomaly at θ = 30° and χ = 0.2 was due to a second nucleation site caused by a surface imperfection and was not related specifically to the channel rotation.

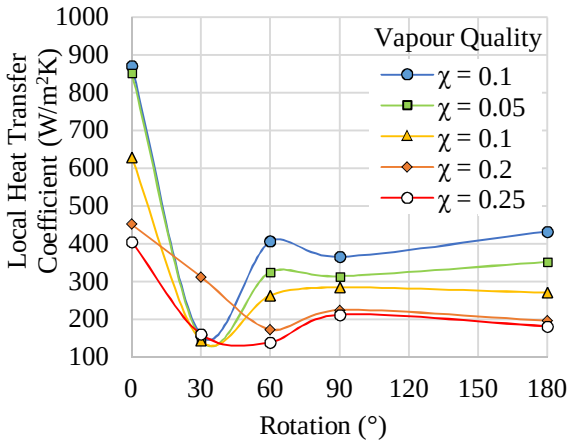

Figure 8: Local heat transfer coefficients in terms of θ at a mass flux of 20 kg/m^{2}s and heat flux of 8 kW/m^2 at various vapour qualities.

For a mass flux of 40 kg/m^{2}s, and an effective heat flux of approximately 25 kW/m^2, Figure 9 exhibits similar trends to those in Figure 8, except that no anomaly was present at θ = 30°. The best heat transfer coefficients were still obtained for bottom heating, irrespective of the reported vapour quality. At vapour qualities of χ = 0 and 0.1, bottom heating resulted in heat transfer coefficients that were 153% and 201% greater than for top heating respectively. Compared with bottom heating, θ = 30° exhibited heat transfer coefficients that were approximately 75% lower than for the bottom-heated cases.

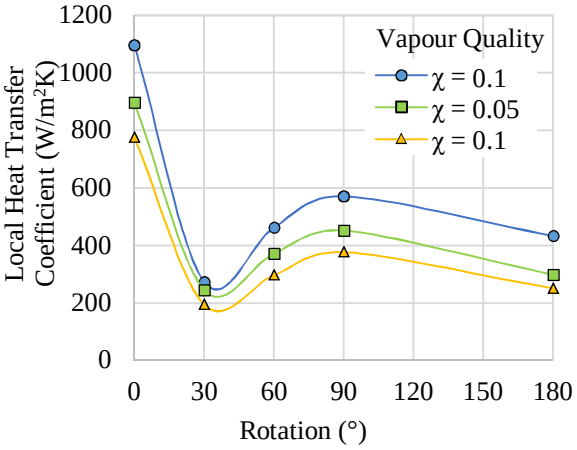

Figure 9: Local heat transfer coefficients in terms of θ rotations at a mass flux of 40 kg/m^{2}s and a heat flux of 12 kW/m^2 at various vapour qualities.

In all three cases above (Figure 7, Figure 8 and Figure 9), the heat transfer coefficient decreased as the vapour quality increased. The figures also indicate that all rotations experienced bubbly, slug or a combination of the two flow patterns typical of flows dominated by nucleate boiling. For cases with θ = 0°, 30°, 60° and 90°, increases in the local heat transfer coefficients were experienced with increases in mass flux, typical of flows dominated by forced convection, while for cases with θ = 180°, the heat transfer coefficient appeared to be independent of mass flux, typical of flows dominated by nucleate boiling.

In Figure 7, Figure 8 and Figure 9 above the effect of mass flux is hard to determine but by comparing vapour qualities of 0 and 0.1 at the above 3 mass flux and heat flux combinations a clear effect can be seen. Figure 10 show the effect of mass flux on the local heat transfer coefficient at all for vapour qualities of 0 and 0.1. It can be seen that the mass flux effects are most pronounced at rotations of 0°, 60° and 90° compared to 30° and 180° which are dominated by only vapour quality effects. A mass flux of 40 kg/m^{2}s resulted in heat transfer coefficients that were up to 26% and 108% higher than for mass fluxes of 20 and 10 kg/m^{2}s at a rotation of 0° and vapour quality of 0. At a rotation of 30° and 180° the difference in the local heat transfer coefficient were almost indistinguishable at the different mass fluxes.

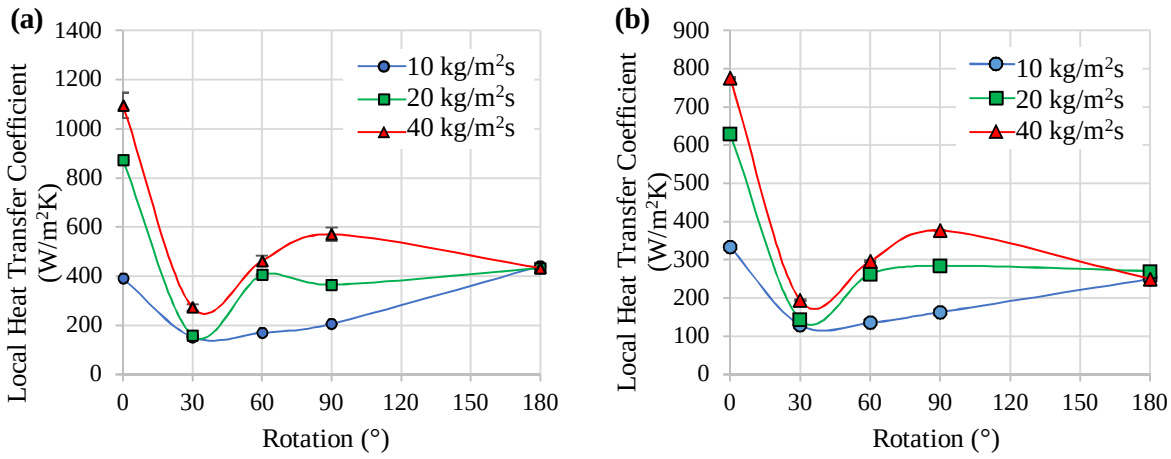

Figure 10: Local heat transfer coefficient in terms of θ rotations of 0°, 30°, 60°, 90° and 180°; at mass fluxes of 10, 20 and 40 kg/m^{2}s and vapour qualities of (a) 0 and (b) 0.1

5.4 Influence of heat flux

Heat flux influences were observed at the point of bubble detachment. Whereas horizontal heating surface orientations (θ = 0° and 180°) had clear bubble detachment, this was not the case for the other orientations. It was found that the local heat transfer coefficient curves at various qualities shifted either upwards or downwards with increases in the heat flux and depended on the dominating flow mechanism. Rotations that were nucleate boiling dominated (θ = 0° and 180°) exhibited increases in the local heat transfer coefficient with increases in the effective heat flux; while for cases that were dominated by forced convection exhibited a decrease in the local heat transfer coefficient with an increase in the effective heat flux. The influence of the heat flux on the local heat transfer coefficient at a mass flux of 10 kg/m^{2}s are presented in Figure 11 (a) and (b) for θ = 0° and 90° respectively. Similar trends were obtained for the other mass fluxes.

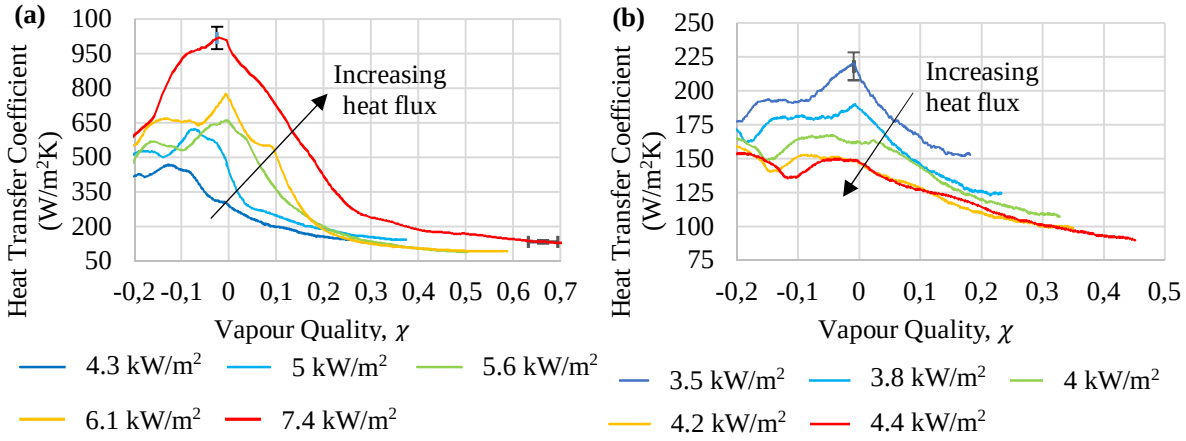

Figure 11: Influence of heat flux on the local heat transfer coefficient at 10 kg/m^{2}s at various vapour qualities for (a) θ = 0° and (b) θ = 90°

Figure 11 (a) indicates that the local heat transfer coefficient curves for θ = 0° were shifted upwards as the heat flux increased, and that the effect is amplified at the highest effective heat flux of $\dot{q}$ = 7.4 kW/m^2. As the heat flux increased, the bubble departure size increased, intensifying the magnitude of the secondary flow induced by bubble motion and producing higher local heat transfer coefficients. For The maximum local heat transfer coefficient occurred with $\dot{q}$ = 7.4 kW/m^2 and was 120% higher than the lowest heat transfer coefficient which occurred with $\dot{q}$ = 4.3 kW/m^2.

For θ = 90° (shown in Figure 11b), the flow behaviour was substantially different from that for θ = 0. There were small peaks in the local heat transfer coefficient at the point of bubble departure, which were suppressed by increases in the heat flux. Increases in the heat flux also shifted the entire local heat transfer coefficient curve downwards.

5.5 Total Pressure Difference

The total pressure difference contains frictional pressure drop, momentum pressure difference, and static pressure difference. Because the system was horizontal for all cases, the static pressure difference in this study was zero. Therefore, the measured pressure difference consisted of frictional pressure drop and momentum pressure change effects. A positive total pressure difference indicated that the pressure at the outlet was higher than the pressure at the inlet, and vice versa. Figure 12 shows the influence of rotation (at the heat flux and mass flux combinations discusses previously) on the total pressure difference. In general, there was a decrease in the total pressure difference as θ increased from 0° to 180°, particularly at a mass flux of 10 and 20 kg/m^{2}s. At a mass flux of 40 kg/m^{2}s at local maximum at θ = 90° was observed.

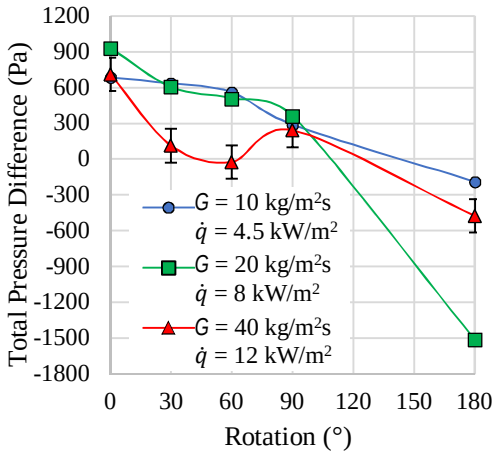

Figure 12: Total pressure difference in terms of θ at various mass and heat flux combinations

The negative total pressure differences observed at 180° indicates that the frictional pressure drop was much larger at this rotation than in the other rotations. It is posited that the other rotations have vapour far away from the heated surface in most cases, and resulted in larger vapour velocities which increased the moment pressure drop. The vapour that moved at higher velocities remained removed from the heated surface and resulted in a less significant increase in the frictional pressure drop.

6. NUMERICAL MODEL

The numerical section of this study focused on the interaction between two incompressible, viscous and Newtonian fluids flowing through a two-dimensional as well as a three-dimensional laminar microchannel using ANSYS® Fluent 19.1. The liquid and vapour phases were modelled as a single fluid using the volume of fluid (VOF) method. In the VOF method, each of the phases was represented by a volume fraction, c, which was equal to 1 in the pure liquid region and equal to 0 in the pure vapour region. The liquid-vapour interface was modelled by smearing the volume fraction over three to four cells, rapidly decreasing it from 0 to 1. The volume fraction was then used in the following equation to create the single-fluid properties, such as density, viscosity and conductivity:

$$\Phi = \Phi_{Liquid} c + (1 - c)\Phi_{vapour} \tag{18}$$

where Φ is an arbitrary scalar and the subscripts $liquid$ and $vapour$ represent the liquid and vapour properties respectively.

The compressive scheme, which recreated the interface from the cell values and normal unit associated with the cell and its surroundings, was used in the propagation and reconstruction of the interface.

6.1 Governing equations

The equations that were solved during each iteration of the solution were idealised forms of the Navier-Stokes equations. The equations for mass, momentum and energy conservation, scalar transport and volume fraction advection are:

$$\nabla(\tilde{u}) = 0 \tag{19}$$

$$\rho\left(\frac{\partial \tilde{u}}{\partial t} + \tilde{u}.\tilde{\nabla}\tilde{u}\right) = -\tilde{\nabla}P + \mu\tilde{\nabla}^2\tilde{u} + \rho g + \sigma\tilde{\kappa}\tilde{n}\delta \tag{20}$$

$$\rho c_p\left(\frac{\partial T}{\partial t} + \tilde{u}.\tilde{\nabla}T\right) = \bar{k}\tilde{\nabla}^2T + \tilde{\nabla}h_{fg}\dot{m} \tag{21}$$

$$\frac{\partial \Phi}{\partial t} + \nabla.\Phi\tilde{u} = \Phi\nabla.\Phi \tag{22}$$

$$\frac{1}{\rho}\left[\frac{\partial}{\partial t}(c\rho) + \nabla.(c\rho\tilde{u})\right] = \frac{1}{\rho}[S_{vapour} - S_{\text{liquid}}] \tag{23}$$

where S_{vapour} and S_{liquid} are volumetric mass source terms (kg/m^{3}s).

6.2 Discretisation methods and solution procedure

Each of the governing equations was solved throughout the domain for every iteration; however, different solving and discretisation methods were used for each aspect. A pressure-based solver was used for all cases in the study, with the PRESTO! (PREssure STaggered Option) method used to calculate the pressure based on a discrete continuity balance. Once the continuity balance was conducted, the pressure and velocity were coupled using the PISO (Pressure-Implicit with Splitting of Operators) method.

Each of the spatial gradients that were used in the governing equations was created using a second-order scheme. A second-order upwind scheme was used for the energy and momentum equations, while a second-order implicit method was used to calculate the volume fraction gradient.

To propagate the solution through time, a first-order implicit time-stepping method was used. Each of the governing equations was iterated through each time step until they converged to 1e^{-4}. A variable time-stepping method was used, which limited the time step via a Courant-Friedrichs-Lewy (CFL) criterion, where the CFL value was set to 0.25. An additional constraint of $\Delta t_{max} < 1e^{-6}$s was used to ensure that no more than 1% of the liquid in a cell could evaporate per time step. These constraints resulted in a time step of between $2e^{-7}$ s and $1e^{-6}$ s.

The model was initially run as a steady-state case to create fully developed velocity, temperature and pressure profiles. A vapour slug, with properties at the saturation temperature, was then patched into the domain. Once the bubble was placed into the microchannel, the domain was changed to transient and the simulation was run utilising a mass transfer user-defined function (UDF) described in Section 5.3. The procedure that was followed to obtain a transient solution is displayed in Figure 13.

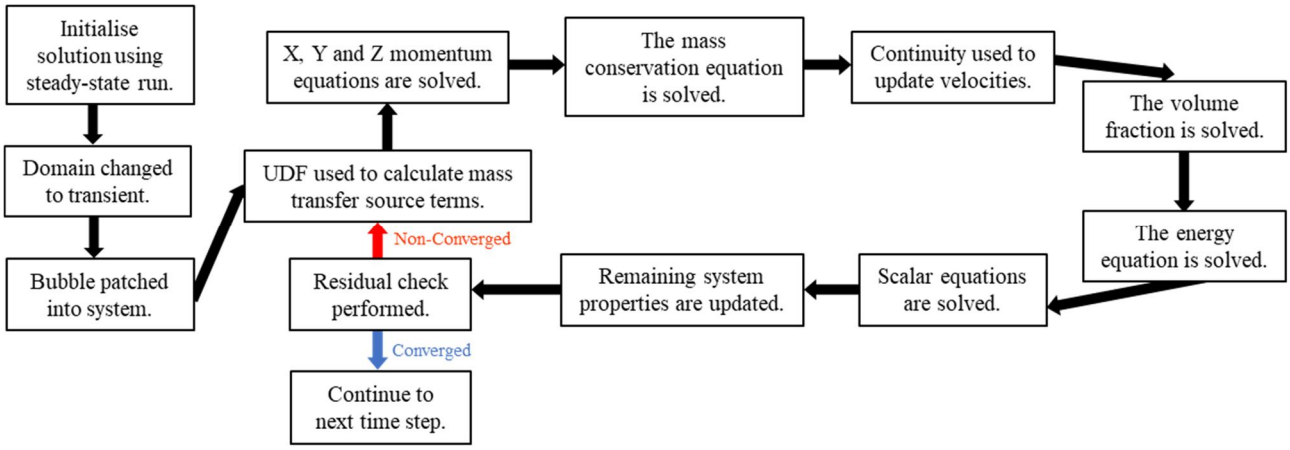

Figure 13: Solution procedure

6.3 Mass transfer

Mass transfer is a critical aspect of flow-boiling modelling. Therefore, it was important to accurately represent it in this study. Mass transfer occurs at the boundary between fluid and vapour and is a microscopic phenomenon, which means that modelling it using finite volumes is inherently flawed. This made it necessary to use an approximation that could be implemented in a computational fluid dynamics (CFD) model.

A mass transfer relation that was devised by Schrage [53] was used as the basis for the mass transfer model. The relation, after being transformed to be better suited to CFD by Tanasawa [54], is shown in equation (24):

$$\dot{\rho}_{tr} = \frac{2\omega}{2-\omega}\sqrt{\frac{M}{2\pi R}}\left[\frac{\rho_{vapour} h_{fg}(T_c - T_{sat})}{T_c}\right] \tag{24}$$

where $\dot{\rho}_{tr}$ is the transfer rate of mass, ω is an accommodation coefficient, which was varied to match validation material, R is a gas constant and M is the molecular mass. The mass transfer source terms were then calculated as a function of the gradient of the volume fraction, which ensured that evaporation only occurred in the interface as follows:

$$S_{vapour} = -S_{liquid} = \dot{\rho}_{tr}|\nabla c| \tag{25}$$

While it is necessary to model mass transfer as only occurring within the interface, implementing it in this region causes errors in the advection of the volume fraction [55]. To avoid this, Hardt, et al. [56] devised a smeared source term model, which calculates the mass transfer via the Tanasawa [54] model, but implements it as a mass generation and a mass disappearance source term that are applied over several cells on the liquid and vapour sides of the interface respectively, as shown in Figure 14.

.

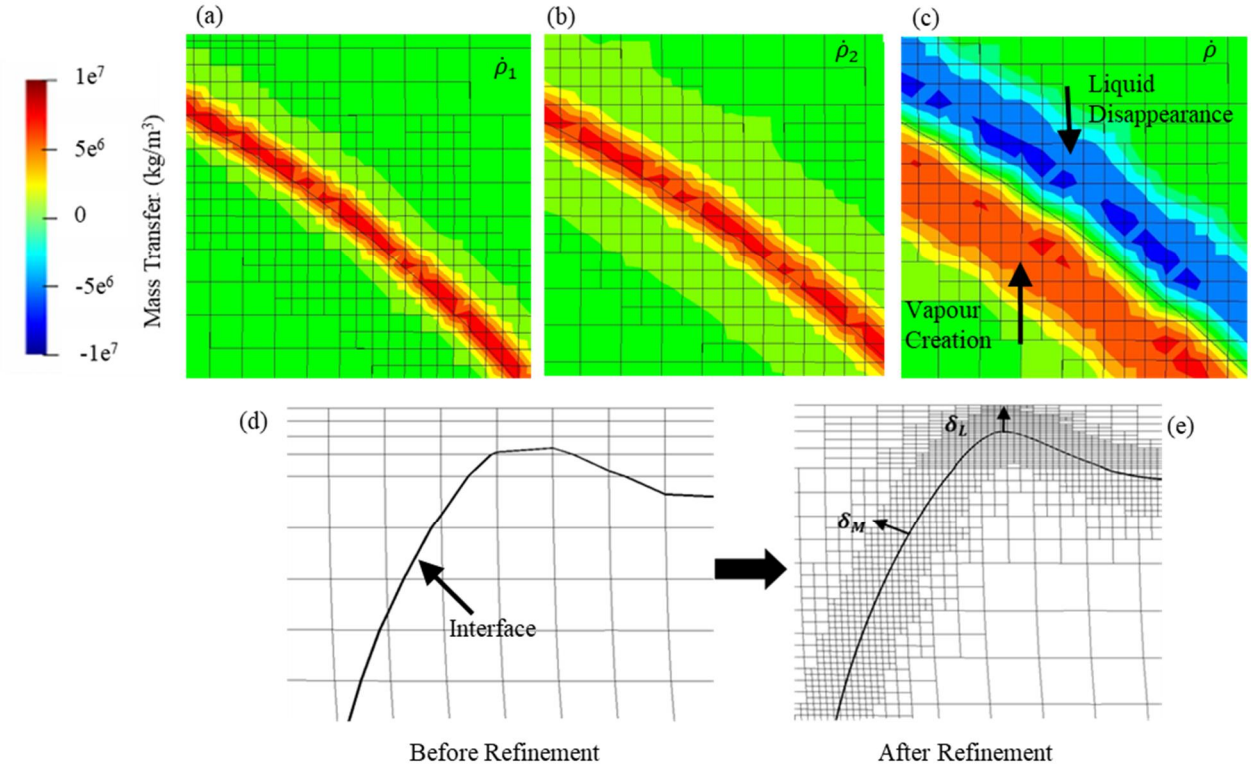

Figure 14: Mass transfer model with initial source term (a), smeared source term (b), implemented source term (c), mesh refinement before implementation (d) and after (e)

The mass transfer model was implemented through a variety of steps, which included the use of a UDF.

Once the solution was initialised, an initial source term was calculated using the mass transfer from equation 26:

$$\dot{\rho}_1 = N_t \dot{\rho}_{tr} c|\nabla c| \tag{26}$$

where N_t is a normalisation factor that ensured that the multiplication of c into the equation did not affect the total mass transfer. The initial source term was then smeared using the following steady Helmholtz equation with Neumann boundary conditions:

$$\dot{\rho}_2 = \dot{\rho}_1 + \Gamma \nabla^2 \dot{\rho}_2 \tag{27}$$

The smeared source term was used to create the source term that was implemented into the model as:

$$\dot{\rho} = \begin{cases} N_{vapour}(1-c)\dot{\rho}_2 & if\ c < 0.001 \\ N_{liquid} c \dot{\rho}_2 & if\ c > 0.999 \\ 0 & if\ 0.001 \leq c \leq 0.999 \end{cases} \tag{28}$$

where N_{vapour} and N_{liquid} are normalisation factors that ensured the total mass transfer was conserved in the vapour and liquid domains respectively. These source terms were then implemented in the pure liquid and vapour regions.

To account for the transfer of sensible heat from the liquid phase to the vapour phase and to account for the latent heat of the fluid, the following energy source term was implemented in the mixture domain:

$$\dot{h} = -\dot{\rho}_1 h_{fg} + N_{vapour}(1-c)\dot{\rho}c_{p,vapour}T_c - N_{liquid}c\dot{\rho}c_{p,liquid}T_c \tag{29}$$

where $\dot{h}$ is the energy source term.

6.4 Adaptive mesh refinement

To increase the resolution around specific areas, adaptive mesh refinement can be done. This method changes specific areas of the mesh at set intervals, either every couple of iterations or every couple of time steps. The default adaption procedure in ANSYS® Fluent can be based on several different parameters, such as pressure or temperature, but for two-phase flow simulations, the more common parameter is the gradient of the volume fraction, which refines cells that are within the interface. This method was used in studies conducted by authors such as Fondelli, et al. [44] and Mehdizadeh, et al. [45].

Because of the spurious currents surrounding the bubble interface, which are characteristic of numerical investigations into flow-boiling in microchannels, only refining the cells at the interface does not properly capture the mass transfer, temperature, surface tension and velocity gradients. The mass transfer that was implemented was also smeared over three to four cells on either side of the interface, and it was imperative for this study that mass transfer only occurred within refined cells. Therefore, it was necessary to refine a set region on either side of the interface, which ensured that these gradients and mass transfer were captured and that the thin liquid film between the bubble and the wall was fully refined.

To ensure that the cells around the interface were fine enough to capture the solution and that refined cells that were no longer in close proximity to the interface were not unnecessarily inducing high computational costs, an execution command was used to implement the refinement every 10 time steps. The method implemented in this study used a UDF to create a region around the interface that was refined to consistently have at least four cells on either side of the interface. This ensured that the spurious currents that existed around the bubbles, as well as the mass transfer, only occurred in refined cells. The number of refined cells on either side of the interface is referred to as δ_M and the refinement level is referred to as δ_L. The refinement level is the number of times each bulk cell is required to be refined before the elements within it are the same size as the cells at the interface. This refinement is displayed in Figure 14.

The reduction in cell count that could be attained from using this model had a major influence on the accuracy of this study. Several benchmark tests which varied the refinement level and refinement area were done. The tests proved that a refinement ratio of three and a minimum of four refined cells on either side of the interface provided accurate results.

7. NUMERICAL VERIFICATION AND VALIDATION

To ensure that the models, methods and boundary conditions correctly represented the physical phenomena in question and that the mesh accurately propagated the solution, several benchmark tests were done and then compared with each

other as well as with two previously published studies. The size of the elements was of particular concern to this study because the small cell size required to correctly capture the effects of surface tension and mass transfer caused the three-dimensional domain to require cell numbers in the range of several hundred million without mesh refinement. The size and mesh refinement model were tested by performing simulations that altered the minimum cell size, the refinement ratio and the number of refined cells on either side of the interface.

The validation was done on a 0.5 x 10 mm axisymmetric domain. A pill-shaped vapour slug was initialised at the base of the channel and then it was allowed to flow through an adiabatic region, which resulted in it developing into a bullet-shaped profile. The microchannel had an inlet mass flux of 600 kg/m^{2}s and a heat flux along the heated region of 9 kW/m^2. The initial, boundary and operating conditions were chosen so that these simulations could be compared with existing studies conducted on the same numerical domain. A fuller description is found in [43] or [42]. The dimensionless location of the bubble, which was used during the validation cases, was defined as the distance from the inlet over the diameter resulting in a channel that is 20D in length, where D = 0.5 mm.

The simulations done varied the size of the cells within the region that contained surface tension and mass transfer with minimum bulk cell sizes ranging from 50 to 17.5 μm and minimum boundary cell sizes from 16 to 4 μm respectively. The heat transfer coefficient along the heated surface at the end of each simulation and the dimensionless location of the front and rear of the bubble throughout the simulations were taken as the metrics of comparison. The heat transfer coefficient for the numerical simulations was calculated in each boundary cell using the equation:

$$\alpha_c = \frac{\dot{q}}{T_h - T_{sat}} \tag{30}$$

where α_c is the cell-based heat transfer coefficient and T_h is the cell-based surface temperature.

The heat transfer coefficient for each of the four cases converged towards a solution at 25 μm, which differed from the smaller cell size of 17.5 μm by a maximum of 4%, which was an acceptable error for a three-dimensional simulation that was particularly sensitive to the cell size.

The dimensionless location of the rear and front of the bubbles for each of the four cases produced closer results than the heat transfer coefficient. There was little difference between the 25 and 17.5 μm cases, with a maximum error of 1.5% between the two. These two sets of results allowed the solution to be judged as converged at a cell size of 25 μm, with the heat transfer, mass transfer and flow dynamics unaffected by the cell size.

Increasing the cell count from 5 500 to 9 000 and from 9 000 to 14 000 caused large changes in the heat transfer coefficient and location of the front of the bubble; however, further increases in the cell count past this produced negligible changes. While increasing the cell count could have decreased the error, the slight increase in accuracy was not worth the large computational cost. This computational cost will be greater in a three-dimensional simulation, where halving the

cell size will increase the cell count by a factor of eight, as opposed to the fourfold increase that occurs in a two-dimensional simulation.

Once the solution was mesh independent, it was compared with previous studies conducted on the same computational domain to ensure that the solver settings and methods produced accurate results. The comparison parameters were the same as those used in the cell size comparisons, which were the heat transfer coefficient at the end of the simulation and the dimensionless locations of the slugs. The heat transfer coefficient in comparison with two previous studies as well as the single-phase solution is shown in Figure 15(a).

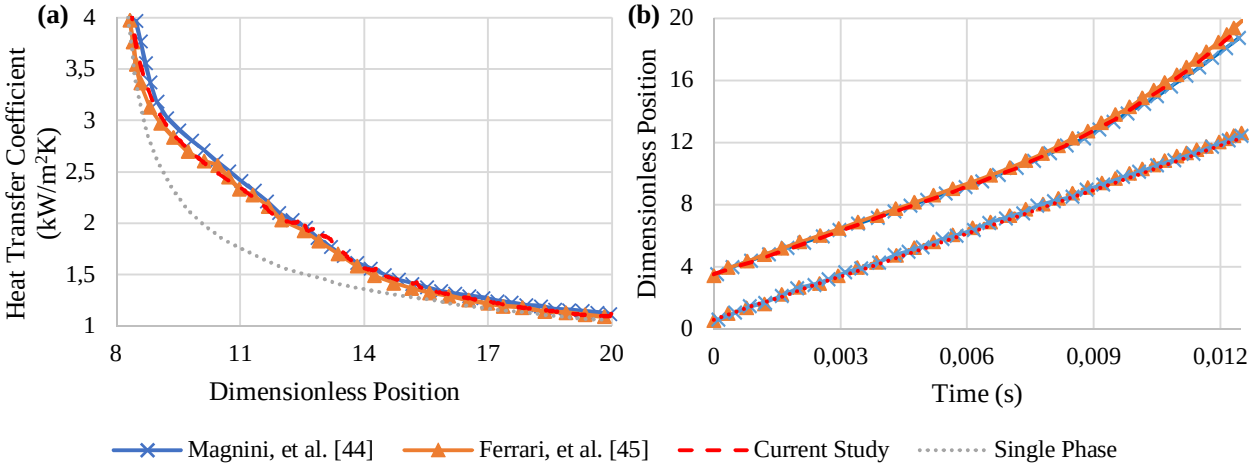

Figure 15: Heat transfer coefficient along the heated surface and dimensionless bubble position compared with previous numerical studies

Figure 15(a) shows that similar results were obtained by all three studies, with negligible differences between the results of this study and those of Ferrari, et al. [43] (6.7%) as well as Magnini, et al. [42] (5.3%). Similar results were obtained when looking at the dimensionless positions of the front and rear of the bubbles, which are shown in Figure 15(b).

There was little difference between the rear of the bubbles in each case, showing that the flow dynamics were replicated. However, there were slightly larger differences between the front of the bubbles produced in this study and that of Ferrari, et al. [43] (2.5%) and Magnini, et al. [42] (3%), which were likely caused by the difference is discretisation methods and solvers.

The mesh independence study, as well as the literature comparison, validated the numerical model used in the current investigation. The error that was introduced via the mesh size, the solver settings and methods was shown to be negligible, while still allowing a three-dimensional model to be developed and run without unreasonable computational costs being involved.

8. NUMERICAL RESULTS

Flow-boiling involves several highly complex microscale phenomena, and therefore numerically modelling this process requires microscale computational cell sizes and time steps. Coalescence, bubble departure and mass transfer are phenomena that are not well understood, with few basic models available to simulate their effect on a system [55]. Because

of this, creating three-dimensional numerical models that simulate each aspect of flow-boiling, such as bubble nucleation, break-off, coalescence and dry-out is extremely computationally expensive. This has resulted in most studies focusing on only one or two aspects of flow-boiling, and usually only in two dimensions. The following sections focus on the growth of a single bubble with varying gravitational orientations and contact angles in a rectangular microchannel in both two and three dimensions.

8.1 Numerical domain

The purpose of the numerical simulations was to give insight into the results obtained in the experimental investigation, which was performed using a section of a microchannel of the same dimensions. The areas of focus were the effects of changing orientation and contact angle on the growth of bubbles and the heat transfer performance. The phenomenon of bubble departure, which is a driving aspect of flow-boiling, was modelled via a changing contact angle model, which reduced the contact angle until the contact area between the vapour bubble and the heated surface reduced to zero. The bubble then detached and joined the flow of the bulk fluid. These results were regarded as the progress into a full-scale flow-boiling model, which would require many more aspects of the flow to be modelled.

To gain a better understanding of the internal mechanisms in operation during flow-boiling in a high aspect ratio microchannel, the numerical model was built to represent flow-boiling of FC-72 in a 10 mm section of the 0.5 x 5 mm rectangular microchannel test section that experienced bubble nucleation and break-off. The domain and the basic boundary conditions are shown in Figure 16, as well as the initial locations of the seeded bubbles (represented by the green and blue semi-circles).

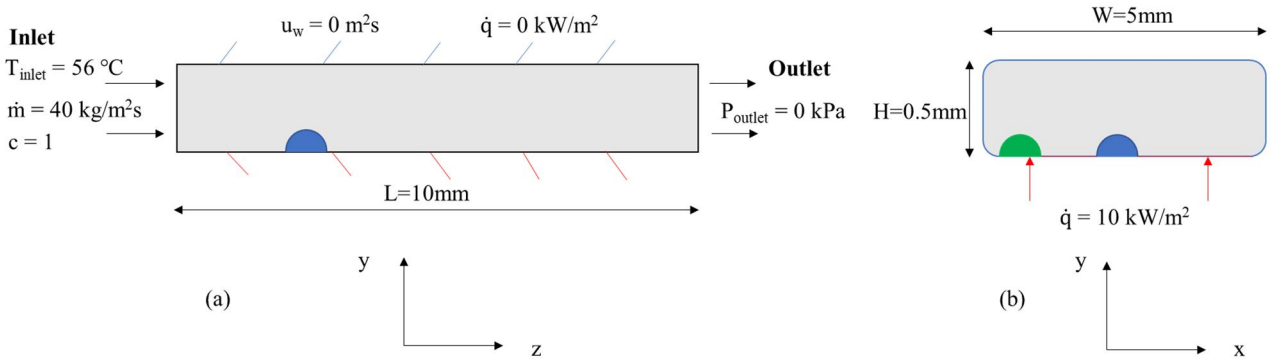

Figure 16: Primary initial and boundary conditions (not drawn to scale)

The two-dimensional cases were run on the same mesh that was used for the validation; however, the domain was transformed to a planar domain and the material properties, boundary and initial conditions were changed to represent a cut-out through the centre of the microchannel, which is graphically represented by Figure 16(a). The domain was then expanded to a three-dimensional domain whose axial and transversal cross-sections are shown in Figure 16(a) and Figure 16(b) respectively. The location of the bubble for the top- (θ = 180°) and bottom- (θ = 0°) heated cases is shown in blue and the location of the seeded bubble for the side- (θ = 90°) heated case is shown in green. The bubble locations were based on the average seeding locations observed during preliminary experimental tests for the 3 orientations being simulated. The simulations were run on a mesh with 25 µm square bulk cells with inflation at the boundaries, which

resulted in boundary cells 6 µm thick. Adaptive mesh refinement was used to refine the area around the bubble interface resulting in bulk cells with uniform dimensions of 3.15 µm and boundary cells with a thickness of 0.75 µm.

8.2 Two-dimensional results

In total, eight two-dimensional cases were conducted to judge the effect of both gravitational orientation and contact angle. Four cases were run with gravity facing upwards and four were run with gravity facing downwards. In each gravitational orientation, four different contact angles were used, which were θ_c = 30°, 45° and 60°, and a detachment case, which started with a contact angle of θ_c = 45° until the bubble started to become confined by the opposing wall (25 ms). Once it started to become confined, the contact angle was gradually reduced to 1° over 20 ms in a method similar to the one used by Sanna, et al. [57] to recreate bubble departure.

During each case, the total bubble area throughout the domain was monitored and is reported in Figure 17 (a), which shows a different growth rate for each gravitational orientation and contact angle. In each case, the top-heated growth rate was slightly higher than the bottom-heated growth rate. However, this difference shrank as the initial contact angle was reduced, with the θ_c = 30° case showing the least difference.

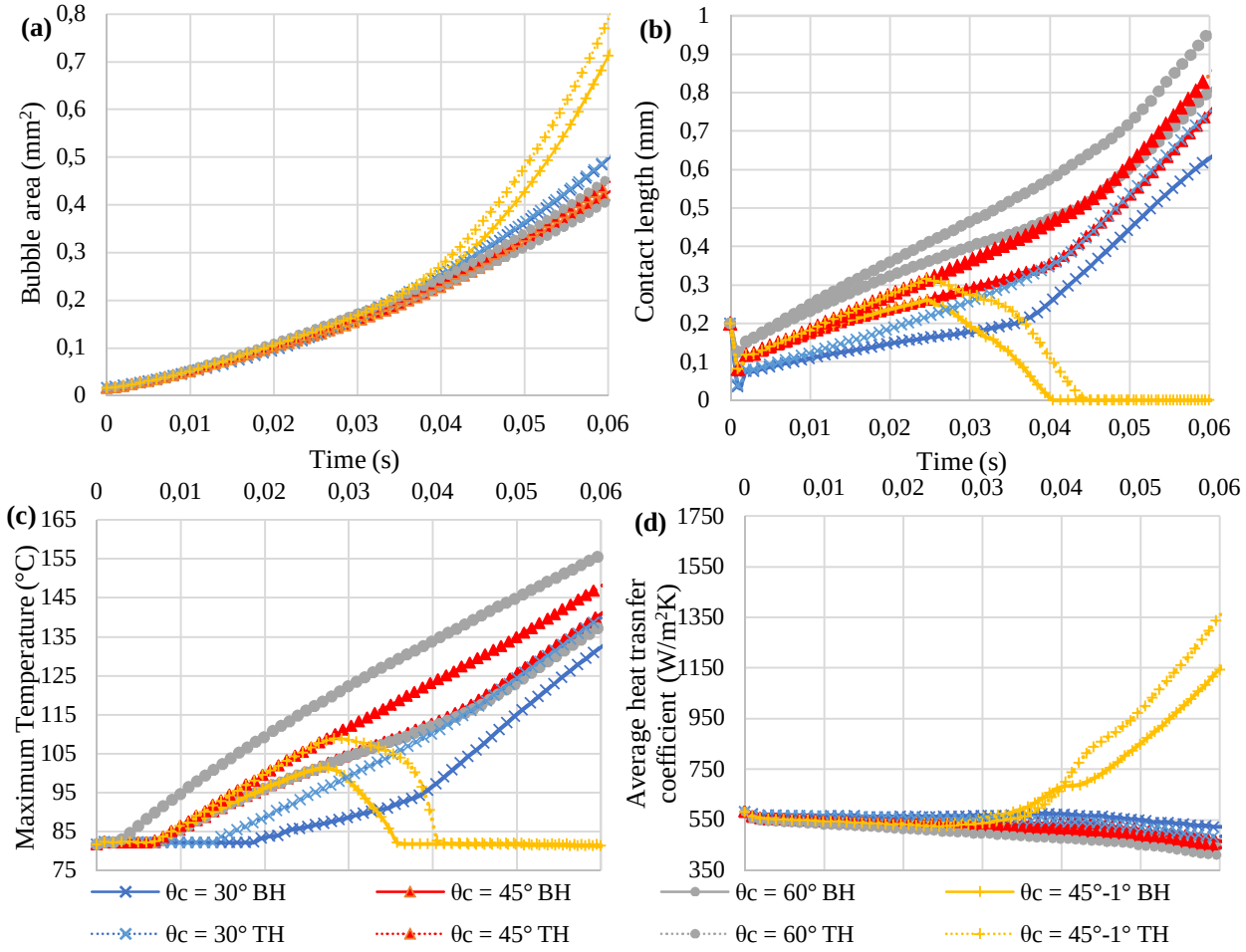

Figure 17: Bubble area (a), contact length (b), maximum temperature (c) and heat transfer coefficient (d) vs time for the bottom-heated (BH) and top-heated (TH) cases at various applied contact angles

The departure of the bubble in the 45°-1° cases is visualised via the contact area between the bubble and the heated surface, shown in Figure 17 (b). The cases originally grew linearly, with a larger growth rate for the top-heated cases. Once the contact angle was reduced, the contact length shrank until it reached 0, at which point the bubble broke free and joined the bulk flow.

The difference between the top- and bottom-heated cases was caused by the force of buoyancy, which squeezed the bubble against the heated surface during the top-heated case and pulled the bubble away from the heated surface during the bottom-heated case. The effect of confinement is also evident in Figure 17 (b). Once the bubble had grown enough to reach the opposing wall, it began to deform and lose its spherical top. Its growth in the axial direction then accelerated, increasing the contact length at a higher rate than before confinement began.

The detachment procedure for the bottom-heated case is shown in Figure 18. Up to 16 ms, the cases were exactly the same; however, at 32 ms, the contact angle reduction had begun, causing a smaller contact angle between the bubble and the heated surface. At 48 ms, the bubble had detached and joined the bulk flow. Once the bubble had grown large enough, dry-out between the bubble and the wall should have begun; however, no model was used to induce this.

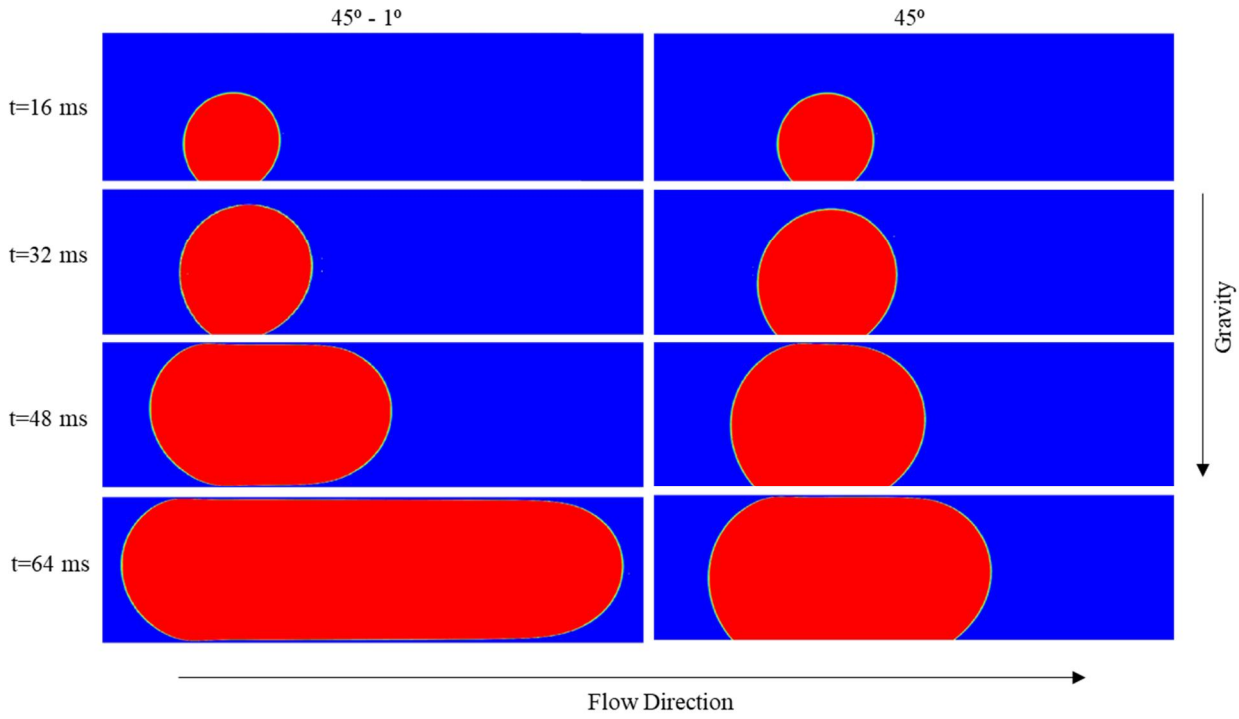

Figure 18: Visualisation of bubble detachment for the bottom-heated case

The maximum temperature that was experienced throughout the domain exhibited a trend that was close to the trends exhibited by the contact length shown in Figure 17 (c) began at the outlet of the channel for each of the cases. However, as more heat was absorbed by the vapour, the location of maximum temperature moved to the contact region between the bubble and the heated surface. For each of the cases, the maximum temperature was larger for the top-heated case than for the bottom-heated case, which was caused by a larger contact length between the bubble and the heated surface. The larger this region was, the larger the distance between the centre of the region and the bubble interface was, which created a larger overall thermal resistance.

Once the contact angle in the detachment cases was reduced, the maximum temperature reduced until it was no longer within the contact region between the bubble and the surface, which had disappeared. The maximum temperature then reverted back to the outlet of the channel, which was slightly lower than it was at the beginning of the simulation due to the increase in forced convection caused by the presence of the growing bubble. This decrease in temperature provided insight into the sudden decrease in temperature shown in Figure 5. As the bubble nucleated, a hotspot was caused by the contact between the heated surface and the vapour. However, as the bubble detached, cooler liquid filled the void left by the bubble, reducing the temperature.

The presence of bubble departure on the heat transfer coefficient of the system can be seen in Figure 17 (d), which shows that once departure began, the average heat transfer coefficient of the heated surface increased significantly. In general, as the contact angle was decreased, the heat transfer coefficient gradually increased. However, once departure began, the heat transfer coefficient rapidly increased, which was due to cooler fluid being sucked underneath the bubble to the superheated region, which was previously occupied by vapour. Once the detachment was complete, the heat transfer coefficient still grew in proportion to the growth rate of the bubble; however, the rate was slower than it was during the detachment phase. The heat transfer coefficient of all the cases without detachment gradually decreased due to the increased size of the contact region between vapour and the heated surface, which is similar to the case shown in Figure 6.

8.3 Three-dimensional results

Once the two-dimensional investigation was completed, three three-dimensional cases were conducted. Two of these cases, the top-heated $\theta_c = 60°$ case and the bottom-heated detachment case, were repeated from the two-dimensional cases. A third case, which was not possible to recreate in two dimensions, was also done. This case had gravity running perpendicular to both the flow direction and the heated surface, which represented heating from the side. The side-heated case had the same contact angle as that of the top-heated case with $\theta_c = 60°$ but had a bubble seeded on the side of the channel rather than in the middle.

The three-dimensional cases produced similar results to those of the two-dimensional cases, with the heat transfer coefficient of the detachment case dwarfing the other two cases. This was due to the process of detachment, which pulled cooler liquid beneath the bubble and quenched the superheated surface. The temporal and spatially averaged heat transfer coefficients for the experimental case with a mass flux of 40 kg/m2s and a heat flux of 13 kW/m2 were compared with the numerical results in Figure 19. The trends shown in Figure 19 matched the trends shown in Figure 6, which indicated a large spike in heat transfer coefficient from the bubble nucleation to the departure zone for the bottom-heated case ($\theta = 0°$). The side-heated ($\theta = 90°$) and top-heated ($\theta = 180°$) cases displayed a relatively steady heat transfer coefficient over these zones in both the experimental and numerical results. The numerical top- and side-heated cases matched up closely with the experimental results, with an error of approximately 6%. The bottom-heated case had a larger error, which was approximately 11%, and was likely caused by the linear bubble departure model that was used.

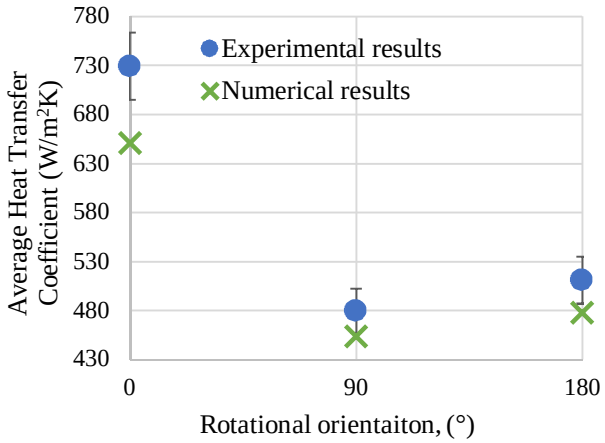

Figure 19: Average heat transfer coefficient during the region between bubble nucleation and departure for experimental results at a mass flux of 40 kg/m^{2}s and heat flux of 13 kW/m^2 and numerical results at 40 kg/m^{2}s and with heat flux 10 kW/m^2

In all three of the three-dimensional cases, the flow throughout the domain was significantly impacted by the presence of the bubble within the flow domain. The impact that the bubble had on the bulk flow was similar for the θ = 0° and 180° heated cases; however, the θ = 90° case had less impact, as demonstrated in Figure 20.

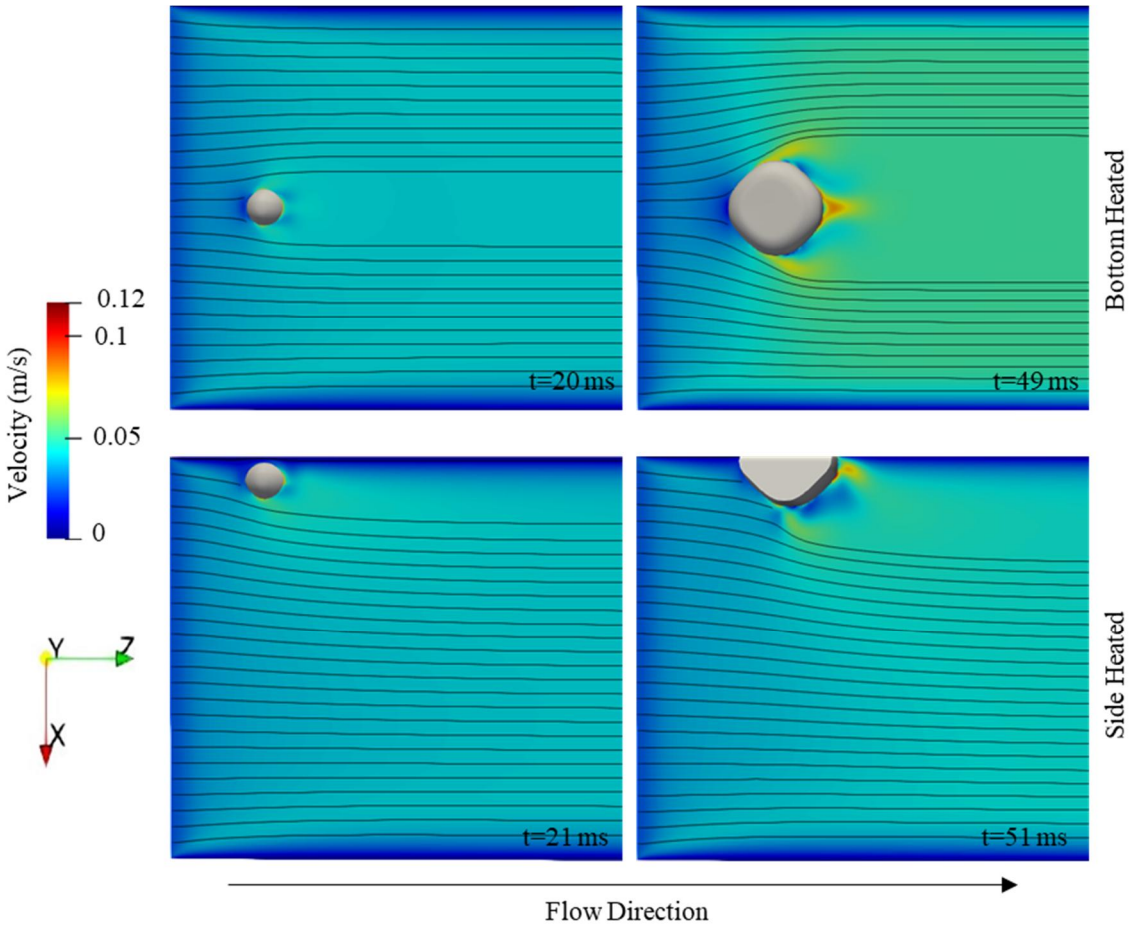

Figure 20: Velocity contours and streamlines of the bottom-heated case and the side-heated case (m/s)

As the bubble grew in size, fluid was forced to flow around it, reducing the flow area and therefore increasing the flow speed. The fluid directly in front of the bubble was also accelerated by the massive increase in volume of the bubble caused by the large density difference between the liquid and vapour.

Figure 20 shows how the presence of the bubble in the bottom-heated case caused liquid acceleration around the side of the bubble, followed by a small region of deceleration as the flow area increased, followed again by a large acceleration of the liquid as the growing bubble pushed the liquid forward. The flow was not only affected near the bubble, but also down the length of the microchannel with large increases in velocity, which increased the forced convection in this region.

The effect of the bubble on the flow was slightly lower for the side-heated (θ = 90°) case. The bubble formed on the side of the channel due to the force of buoyancy, which placed it in a region where a velocity boundary layer had formed. This boundary layer can be seen in Figure 20. Therefore, the effect of the bubble on the downstream flow was approximately 40% less than for the bottom-heated (θ = 0°) case and only occurred at one side of the channel, which further influenced the difference in heat transfer coefficient between the bottom- (θ = 0°) and side- (θ = 90°) heated cases, as shown in Figure 6.

Both the two- and three-dimensional results showed that the gravitational orientation of the channel affected the heat transfer characteristics of the domain, mostly through the influence that it, as well as the contact angle, had on the departure of the nucleated bubbles. The gravitational orientation also had an effect on the location of nucleated bubbles, which influenced the extent to which these bubbles affected the bulk fluid flow.

9. CONCLUSION

A joint experimental and numerical investigation of flow-boiling was conducted focusing on the effect of rotation on the local time-averaged heat transfer coefficient in a mini/micro channel with an aspect ratio of 10 and hydraulic diameter of 909 μm. The experimental results showed that bubble detachment from a nucleation site had a significant impact on the local heat transfer coefficient. Bottom-heated cases (θ = 0°) had a nucleation site with clear bubble growth and detachment, which improved the local heat transfer coefficient by up to 201% compared with other rotations at all vapour qualities and mass fluxes. Channels with rotational orientation of θ = 0° and 180° were dominated by nucleate boiling with an increase in the local heat transfer coefficient as heat fluxes increased and more intense boiling occurred at nucleation. Rotated channels (θ = 30°, 60° and 90°) had a combination of flow behaviour dominated by nucleate boiling and forced convection with a decrease in the local heat transfer coefficient as vapour quality increased but also a decrease in the local heat transfer coefficient with an increase in the heat flux. The numerical simulations supported the results of the experimental investigation, showing that the gravitational orientation of the channel had a large effect on the heat transfer characteristics of the microchannel. The average heat transfer coefficient of the θ = 0° heated case increased during bubble departure to almost 100% higher than for the θ = 180° heated case. The θ = 90° heated case showed the least impact of the bubble on the average heat transfer coefficient, which increased by only 2% over the duration of the simulation. Additional experimental work is needed to determine what the critical mass flux the effect the localised buoyancy driven become insignificant.

Acknowledgements

This project has received funding from the European Union's Horizon 2020 research and innovation programme under the Marie Skłodowska-Curie grant agreement No. 778104. The authors also acknowledge the Centre for High Performance Computing (CHPC), South Africa, for providing computational resources for this research project.

References

[1] K. Strąk, M. Piasecka, B. Maciejewska, Spatial orientation as a factor in flow boiling heat transfer of cooling liquids in enhanced surface minichannels, International Journal of Heat and Mass Transfer, 117 (2018) 375-387.

[2] P.A. Kew, K. Cornwell, Correlations for the prediction of boiling heat transfer in small-diameter channels, Applied Thermal Engineering, 17(8) (1997) 705-715.

[3] L. Cheng, G. Xia, Fundamental issues, mechanisms and models of flow boiling heat transfer in microscale channels, International Journal of Heat and Mass Transfer, 108 (2017) 97-127.

[4] J.M. Li, B.X. Wang, Size effect on two-phase regime for condensation in micro/mini tubes, Heat Transfer - Asian Research, 32(1) (2003) 65-71.

[5] 3M, 3M Fluorinert Electronic Liquid FC-72 TDS_FINAL.pdf, (2019).

[6] L.-H. Chien, W.-R. Liao, M. Ghalambaz, W.-M. Yan, Experimental study on convective boiling flow and heat transfer in a microgap enhanced with a staggered arrangement of nucleated micro-pin-fins, International Journal of Heat and Mass Transfer, 144 (2019) 118653.

[7] L. Gao, S.H. Bhavnani, Experimental study of augmented flow boiling in a dielectric fluid due to backward and forward facing stepped microchannels, International Journal of Heat and Mass Transfer, 124 (2018) 484-490.

[8] W.-R. Liao, L.-H. Chien, M. Ghalambaz, W.-M. Yan, Experimental study of boiling heat transfer in a microchannel with nucleated-shape columnar micro-pin-fins, International Communications in Heat and Mass Transfer, 108 (2019) 104277.

[9] L.-H. Chien, W.-R. Liao, M. Ghalambaz, W.-M. Yan, Experimental study on convective boiling of micro-pin-finned channels with parallel arrangement fins for FC-72 dielectric fluid, International Journal of Heat and Mass Transfer, 138 (2019) 390-400.

[10] A. Iqbal, M. Pandey, A simple methodology to incorporate flashing and variation of thermophysical properties for flow boiling pressure drop in a microchannel, International Journal of Thermal Sciences, 132 (2018) 137-145.

[11] K. Strak, M. Piasecka, B. Maciejewska, Comparison of the 1D and 2D calculation models used for determination of the heat transfer coefficient during flow boiling heat transfer in a minichannel, E3S Web Conf., 128 (2019) 01017.

[12] M. Piasecka, K. Strąk, Influence of the Surface Enhancement on the Flow Boiling Heat Transfer in a Minichannel, Heat Transfer Engineering, 40(13-14) (2019) 1162-1175.

[13] K.K. Wong, K.C. Leong, Nucleate flow boiling enhancement on engineered three-dimensional porous metallic structures in FC-72, Applied Thermal Engineering, 159 (2019) 113846.

[14] B. Yuan, Y. Zhang, L. Liu, J. Wei, Experimental research on subcooled flow boiling heat transfer performance and associated bubble characteristics under pulsating flow, Applied Thermal Engineering, 157 (2019) 113721.

[15] Y. Wang, K. Sefiane, S. Harmand, Flow boiling in high-aspect ratio mini- and micro-channels with FC-72 and ethanol: Experimental results and heat transfer correlation assessments, Experimental Thermal and Fluid Science, 36 (2012) 93-106.

[16] S. Korniliou, C. Mackenzie-Dover, S. Harmand, G. Duursma, J.R.E. Christy, J.G. Terry, A.J. Walton, K. Sefiane, Local wall temperature mapping during flow boiling in a transparent microchannel, International Journal of Thermal Sciences, 135 (2019) 344-361.

[17] S. Korniliou, C. Mackenzie-Dover, J.R.E. Christy, S. Harmand, A.J. Walton, K. Sefiane, Two-dimensional heat transfer coefficients with simultaneous flow visualisations during two-phase flow boiling in a PDMS microchannel, Applied Thermal Engineering, 130 (2018) 624-636.

[18] C.M.M. Dover, Y. Li, S. Korniliou, K. Sefiane, J.G. Terry, A.J. Walton, Polydimethylsiloxane (PDMS)-based microfluidic channel with integrated commercial pressure sensors, in: 2017 IEEE SENSORS, 2017, pp. 1-3.

[19] S. Korniliou, Experimental study on local heat transfer coefficients and the effect of aspect ratio on flow boiling in a microchannel, (2018).

[20] W. Li, Z. Chen, J. Li, K. Sheng, J. Zhu, Subcooled flow boiling on hydrophilic and super-hydrophilic surfaces in microchannel under different orientations, International Journal of Heat and Mass Transfer, 129 (2019) 635-649.

[21] O.S. Al-Yahia, T. Kim, D. Jo, Flow Instability (FI) for subcooled flow boiling through a narrow rectangular channel under transversely uniform and non-uniform heat flux, International Journal of Heat and Mass Transfer, 125 (2018) 116-128.

[22] Q. Huang, L. Jia, C. Dang, L. Yang, Experimental Study on Flow Boiling of Deionized Water in a Horizontal Long Small Channel, Journal of Thermal Science, 27(2) (2018) 157-166.

[23] J. Lee, Y. Joo, S.J. Kim, Effects of the number of turns and the inclination angle on the operating limit of micro pulsating heat pipes, International Journal of Heat and Mass Transfer, 124 (2018) 1172-1180.

[24] M.C. Vlachou, T.D. Karapantsios, Effect of channel inclination on heat transfer and bubble dynamics during subcooled flow boiling, International Journal of Thermal Sciences, 124 (2018) 484-495.

[25] J. Barber, D. Brutin, K. Sefiane, J.L. Gardarein, L. Tadrist, Unsteady-state fluctuations analysis during bubble growth in a "rectangular" microchannel, International Journal of Heat and Mass Transfer, 54(23-24) (2011) 4784-4795.

[26] J. Barber, D. Brutin, K. Sefiane, L. Tadrist, Bubble confinement in flow boiling of FC-72 in a "rectangular" microchannel of high aspect ratio, Experimental Thermal and Fluid Science, 34(8) (2010) 1375-1388.

[27] J. Barber, K. Sefiane, D. Brutin, L. Tadrist, Hydrodynamics and heat transfer during flow boiling instabilities in a single microchannel, Applied Thermal Engineering, 29(7) (2009) 1299-1308.

[28] P. Vasileiadou, K. Sefiane, T.G. Karayiannis, J.R.E. Christy, Flow boiling of ethanol/water binary mixture in a square mini-channel, Applied Thermal Engineering, 127 (2017) 1617-1626.

[29] B. Citarella, G. Lillo, R. Mastrullo, A.W. Mauro, L. Viscito, Experimental investigation on flow boiling heat transfer and pressure drop of refrigerants R32 and R290 in a stainless steel horizontal tube, Journal of Physics: Conference Series, 1224 (2019) 012041.

[30] Y. Zhang, R. Tian, X. Dai, D. Wang, Y. Ma, H. Li, L. Shi, Experimental study of R134a flow boiling in a horizontal tube for evaporator design under typical Organic Rankine Cycle pressures, International Journal of Heat and Fluid Flow, 71 (2018) 210-219.

[31] C. Vlasie, H. Macchi, J. Guilpart, B. Agostini, Flow boiling in small diameter channels, International Journal of Refrigeration, 27(2) (2004) 191-201.

[32] T. Wen, H. Zhan, L. Lu, D. Zhang, Experimental investigation and development of new correlation for flow boiling heat transfer in mini-channel, International Journal of Thermal Sciences, 129 (2018) 209-217.

[33] S. Saitoh, H. Daiguji, E. Hihara, Correlation for boiling heat transfer of R-134a in horizontal tubes including effect of tube diameter, International Journal of Heat and Mass Transfer, 50(25-26) (2007) 5215-5225.

[34] L. Cheng, D. Mewes, Review of two-phase flow and flow boiling of mixtures in small and mini channels, International Journal of Multiphase Flow, 32(2) (2006) 183-207.

[35] X. Mingchen, J. Li, D. Chao, P. Qi, The effect of heating direction on flow boiling heat transfer of R134a in Micro-channels, Thermal Science, 26(2) (2017) 166-147.

[36] R. Ajith Krishnan, K.R. Balasubramanian, S. Suresh, The effect of heating area orientation on flow boiling performance in microchannels heat sink under subcooled condition, International Journal of Heat and Mass Transfer, 110 (2017) 276-293.

[37] R. Ajith Krishnan, K.R. Balasubramanian, S. Suresh, Experimental investigation of the effect of heat sink orientation on subcooled flow boiling performance in a rectangular microgap channel, International Journal of Heat and Mass Transfer, 120 (2018) 1341-1357.

[38] S. Szczukiewicz, M. Magnini, J.R. Thome, Proposed models, ongoing experiments, and latest numerical simulations of microchannel two-phase flow boiling, International journal of multiphase flow, 59 (2014) 84-101.

[39] A. Bordbar, A. Taassob, A. Zarnaghsh, R. Kamali, Slug flow in microchannels: Numerical simulation and applications, Journal of industrial and engineering chemistry, (2018).

[40] J. Thome, V. Dupont, A.M. Jacobi, Heat transfer model for evaporation in microchannels. Part I: presentation of the model, International Journal of Heat and Mass Transfer, 47(14-16) (2004) 3375-3385.

[41] M. Magnini, J. Thome, A CFD study of the parameters influencing heat transfer in microchannel slug flow boiling, International Journal of Thermal Sciences, 110 (2016) 119-136.

[42] M. Magnini, B. Pulvirenti, J.R. Thome, Numerical investigation of hydrodynamics and heat transfer of elongated bubbles during flow boiling in a microchannel, International Journal of Heat and Mass Transfer, 59 (2013) 451-471.

[43] A. Ferrari, M. Magnini, J.R. Thome, Numerical analysis of slug flow boiling in square microchannels, International Journal of Heat and Mass Transfer, 123 (2018) 928-944.

[44] T. Fondelli, A. Andreini, B. Facchini, Numerical Simulation of Dam-Break Problem Using an Adaptive Meshing Approach, 2015.

[45] A. Mehdizadeh, S.A. Sherif, W.E. Lear, Numerical simulation of thermofluid characteristics of two-phase slug flow in microchannels, International Journal of Heat and Mass Transfer, 54(15) (2011) 3457-3465.

[46] L.-C. Hsu, S.-W. Cion, K.-W. Lin, C.-C. Wang, An experimental study of inclination on the boiling heat transfer characteristics of a micro-channel heat sink using HFE-7100, International Communications in Heat and Mass Transfer, 62 (2015) 13-17.

[47] A. Mukherjee, S. Kandlikar, Z. Edel, Numerical study of bubble growth and wall heat transfer during flow boiling in a microchannel, International Journal of Heat and Mass Transfer, 54(15-16) (2011) 3702-3718.

[48] K. Ling, G. Son, D.-L. Sun, W.-Q. Tao, Three dimensional numerical simulation on bubble growth and merger in microchannel boiling flow, International Journal of Thermal Sciences, 98 (2015) 135-147.

[49] Y. Wang, K. Sefiane, Effects of heat flux, vapour quality, channel hydraulic diameter on flow boiling heat transfer in variable aspect ratio micro-channels using transparent heating, International Journal of Heat and Mass Transfer, 55(9-10) (2012) 2235-2243.

[50] O. Engineering, Pressure Transducers, (2018).

[51] R.P. Madding, Emissivity measurement and temperature correction accuracy considerations, in: AeroSense '99, SPIE, 1999, pp. 9.

[52] R.J. Moffat, Describing the uncertainties in experimental results, Experimental Thermal and Fluid Science, 1(1) (1988) 3-17.

[53] R.W. Schrage, A theoretical study of interphase mass transfer, Columbia University Press, 1953.

[54] I. Tanasawa, Advances in condensation heat transfer, in: Advances in heat transfer, Elsevier, 1991, pp. 55-139.

[55] C.R. Kharangate, I. Mudawar, Review of computational studies on boiling and condensation, International Journal of Heat and Mass Transfer, 108 (2017) 1164-1196.

[56] S. Hardt, F. Wondra, Evaporation model for interfacial flows based on a continuum-field representation of the source terms, Journal of Computational Physics, 227(11) (2008) 5871-5895.

[57] A. Sanna, C. Hutter, H. Lin, K. Sefiane, A. Walton, E. Pavlovic, I. Golobic, R. A Nelson, T. Karayiannis, D. B R Kenning, Simulation and experimental investigation of pool boiling on a silicon wafer with artificial nucleation sites, 2008.